

A whole-brain model of amyloid beta accumulation and cerebral hypoperfusion in Alzheimer's disease

Mattia Corti ^{1,2}, Andrew Ahern ³, Alain Goriely ³, Ellen Kuhl ^{4,5}, and Paola F. Antonietti ¹

¹MOX-Dipartimento di Matematica, Politecnico di Milano, Milan, Italy

²Faculty of Mathematics, University of Vienna, Oskar-Morgenstern-Platz 1, 1090 Vienna, Austria

³Mathematical Institute, University of Oxford, Oxford, UK

⁴Institute of Applied Mechanics, Friedrich-Alexander-Universität Erlangen-Nürnberg, Erlangen, Germany

⁵Department of Mechanical Engineering, Stanford University, Stanford, CA, USA

Abstract

Accumulation of amyloid beta proteins is a defining feature of Alzheimer's disease, and is usually accompanied by cerebrovascular pathology. Evidence suggests that amyloid beta and cerebrovascular pathology are mutually reinforcing; in particular, amyloid beta suppresses perfusion by constricting capillaries, and hypoperfusion promotes the production of amyloid beta. Here, we propose a whole-brain model coupling amyloid beta and blood vessel through a hybrid model consisting of a reaction–diffusion system for the protein dynamics and porous–medium model of blood flow within and between vascular networks: arterial, capillary and venous. We discretize the resulting parabolic–elliptic system of PDEs by means of a high-order discontinuous Galerkin method in space and an implicit Euler scheme in time. Simulations in realistic brain geometries demonstrate the emergence of multistability, implying that a sufficiently large pathogenic protein seeds is necessary to trigger disease outbreak. Motivated by the ‘two-hit vascular hypothesis’ of Alzheimer's disease that hypoperfusive vascular damage triggers amyloid beta pathology, we also demonstrate that localized hypoperfusion, in response to injury, can destabilize the healthy steady state and trigger brain-wide disease outbreak.

1 Introduction

Alzheimer's disease (AD) is a progressive neurodegenerative disorder characterized by neuronal loss and impaired synaptic communication. It has long been established that the spread of misfolded, prion-like proteins plays a central role in AD and related disorders [54]. In particular, disease onset is associated with the accumulation of two pathological proteins: amyloid-beta (A β) and tau [22]. Cerebrovascular abnormalities frequently accompany AD pathology—for instance, cerebral amyloid angiopathy occurs in more than 90% of AD cases [27], and reductions in cerebral blood flow (CBF) represent one of the earliest measurable biomarkers of the disease [28].

The interplay between A β and cerebral blood flow is well documented. A β acts as a vasoconstrictor, increasing vascular resistance and thereby reducing CBF [62, 45]. Oligomeric A β induces the release of vasoconstrictive agents such as endothelin-1 and generates oxidative stress, which can result in capillary occlusion [15, 46]. Conversely, hypoxia accelerates amyloid precursor protein (APP) processing and impairs its clearance across the blood–brain barrier, promoting A β accumulation [36, 60]. Hypoperfusion-induced injury can further exacerbate APP aggregation, possibly as a compensatory mechanism [58, 25]. Collectively, these mechanisms give rise to a positive feedback loop between A β buildup and vascular dysfunction [26, 32, 36]. Several studies even suggest that vascular damage may act as an early trigger for A β pathology in AD [69, 35].

Mathematical models. In recent years, several mathematical models for the dynamics of *prion-like* proteins have been proposed. The description of the phenomena requires models based on partial differential equations (PDEs) able to describe both the temporal and the spatial dynamics of the phenomena, typically at organ scale. One example developed to describe the dynamics of A β are the Smoluchowski-type models [6, 19], which are derived from microscopical interactions and distinguishes different sizes of pathological aggregates [21]. Some simplified models focus on the interactions between healthy and misfolded proteins, such as the heterodimer model [20, 44], or only on the misfolded proteins population, such as the Fisher–Kolmogorov equation [66]. These simplified models have the advantage that they can be fully validated against existing data and correctly predict the evolution of the disease at personalized and regional levels [9]. They have also been extended to describe connections with

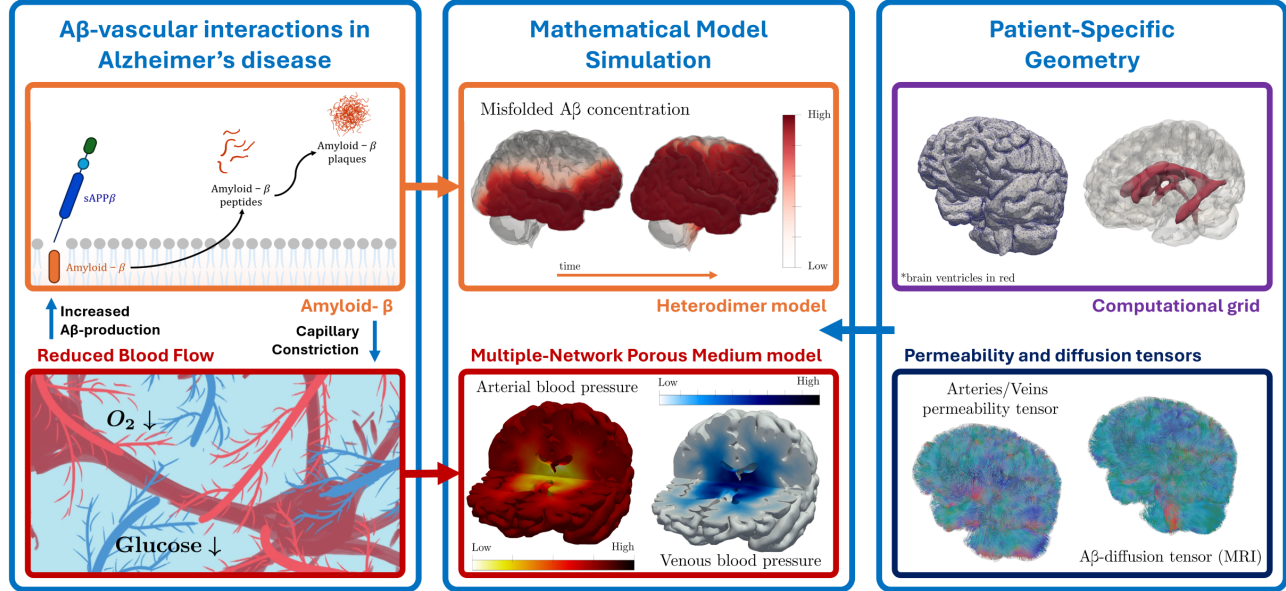


Figure 1: Synthetic representation of the article structure. Description of the A β –vascular interaction in AD (left panel), patients-specific geometry (right panel), and mathematical models and resulting numerical simulations (center panel).

other physical phenomena occurring in AD. For example, the elastic deformations due to atrophy [56, 67, 47], the clearance mechanisms [7], the interactions with tau proteins [63], and brain activity [24, 3].

However, little attention has been devoted to the development of models coupling A β and CBF. In [1], the authors propose a modification of the heterodimer model on networks which takes into account CBF reduction. The first goal of the current work is to build on this idea by developing a continuous PDE model of A β accumulation in the brain describing also the interactions with the cerebral microvasculature through (a) vasoconstriction and (b) perfusion-dependent A β production and clearance (see Figure 1). Our model is based on the heterodimer model for the A β -dynamics description and on a multiple-network porous-medium model for the blood perfusion.

Porous-medium models have been extensively used in the context of brain poromechanics to study strokes [31, 29, 30]. Moreover, a poroelastic version of those models have been proposed to study the brain hemodynamics on the heartbeat scale [11, 38, 49, 64], and clearance mechanisms [40, 65].

In our model, we analyze the impact of A β on the blood flow in the capillaries, altering transfer between compartments and capillaries permeability.

Numerical methods and patient-specific simulations. The potential clinical utility of the constructed mathematical models strongly depend on the design quality of numerical methods to simulate PDEs in patient-specific geometries. In the context of proteinopathies, connectome graph-based simulations for the models introduced in the previous section have been fully implemented [1, 7, 13, 20, 63]. However, the construction of a graph-based model for our purposes would suffer from the limitation of describing the brain's microvasculature as a collection of small independent capillary networks, losing the coupling with the complete vasculature structure at the organ level [1].

To study physical effects in the brain, multiple works have introduced numerical discretizations of PDEs in brain geometries based on continuous finite elements [8, 38, 49, 65] and discontinuous Galerkin (dG) methods [4, 14, 11, 12, 47]. The advantage of using these high-fidelity discretizations is the possibility of constructing patient-specific computational grids from medical images and taking into account geometrical and functional information in the PDE model.

For our mathematical model, we propose a discretization based on a discontinuous Galerkin method in space and implicit Euler time stepping in time. The dG methods provide numerous advantages in our context. Indeed, they are naturally oriented to high-order approximations that are of primary importance for the heterodimer system, which typically admits travelling-wave solutions [34, 4, 10]. Moreover, the construction of a dG method allows local adjustment of the polynomial degree p , which is useful to maintain a low computational cost [39]. Additionally,

they allow the use of polygonal mesh elements which is particularly useful to reduce computational costs in brain applications. Indeed, using mesh agglomeration strategies [5], the complex boundary and internal interfaces can be accurately described with a low number of mesh elements. Concerning the time discretization, the implicit Euler method is combined with a loosely-coupled strategy to solve the parabolic (heterodimer model) and elliptic (multiple-network porous-medium model) parts of the system separately.

In this work, we first carry out simulations in simplified geometries to study and understand the fundamental properties of our mathematical model. Then we perform realistic numerical simulations in brain geometries. In particular, we show the existence of multiple stable states starting from different levels of initial seeding of A β . Finally, we evaluate the injury-induced initiation of AD pathology, by imposing different levels of initial hypoperfusion in the frontal lobe.

Structure of the manuscript. Section 2 is dedicated to the mathematical development of our model. We start from the presentation of the heterodimer model for A β spreading in Section 2.1 and the multiple-network porous-medium model in Section 2.2. Then, in Section 2.3, we propose a novel coupled mathematical model to describe the connections between A β and CBF and in Section 2.4 we derive the weak formulation of the system. In Section 3 we introduce the discretization of the problem based on a dG-space discretization and implicit Euler time stepping. In Section 4, we present numerical simulations in simple geometries to validate the numerical solver and analyze properties of the mathematical model. In Section 5, we simulate the system in realistic three-dimensional brain geometries to study both the multistability of the system depending on the magnitude of the initial seeding and the hypoperfusion-induced pathology. Finally, in Section 6, we conclude and discuss further developments.

2 Mathematical model

2.1 Heterodimer model

We adapt Prusiner's heterodimer prion model [50] for the protein kinetics of A β . That is, we assume that A β monomers can be either normal or pathogenic, with concentrations $u = u(\mathbf{x}, t)$ and $\tilde{u} = \tilde{u}(\mathbf{x}, t)$, respectively. Pathogenic monomers can bind to normal monomers to form a pathogenic–normal heterodimer, which then dissociates into two pathogenic monomers. We assume that the dissociation step is fast and treat this conversion process as a single second-order chemical reaction, with rate k_{12} . Normal proteins are produced at rate k_0 and cleared at rate k_1 , and pathogenic proteins are cleared at rate \tilde{k}_1 .

The resulting reaction–diffusion system with zero-flux boundary conditions is given by:

$$\begin{cases} \frac{\partial u}{\partial t} = \nabla \cdot (\mathbf{D} \nabla u) - k_1 u - k_{12} u \tilde{u} + k_0, & \text{in } \Omega \times (0, T], \\ \frac{\partial \tilde{u}}{\partial t} = \nabla \cdot (\mathbf{D} \nabla \tilde{u}) - \tilde{k}_1 \tilde{u} + k_{12} u \tilde{u}, & \text{in } \Omega \times (0, T], \\ (\mathbf{D} \nabla u) \cdot \mathbf{n}_\Omega = 0, \quad (\mathbf{D} \nabla \tilde{u}) \cdot \mathbf{n}_\Omega = 0, & \text{on } \partial\Omega \times (0, T], \\ u(\mathbf{x}, 0) = u_0(\mathbf{x}), \quad \tilde{u}(\mathbf{x}, 0) = \tilde{u}_0(\mathbf{x}), & \text{in } \Omega, \end{cases} \quad (1)$$

where \mathbf{D} is the diffusion tensor, Ω is the spatial domain (i.e. the brain), \mathbf{n}_Ω is a boundary normal, and u_0, \tilde{u}_0 are the initial protein concentrations. The model thus comprises an initial–boundary value problem for a parabolic system of two PDEs coupled by a nonlinear term.

The spatial transport of A β proteins is a combination of diffusion in the extracellular space and axonal transport. Following [67, 66], we model this combination as anisotropic diffusion whose principal direction is aligned with the brain's axon fibers:

$$\mathbf{D}(\mathbf{x}) = d_{\text{ext}} \mathbf{I} + d_{\text{axn}} \bar{\mathbf{a}}(\mathbf{x}) \otimes \bar{\mathbf{a}}(\mathbf{x}) = d_{\text{ext}} \mathbf{I} + d_{\text{axn}} \mathbf{D}_{\text{axn}}(\mathbf{x}). \quad (2)$$

The vector field of fiber directions, $\bar{\mathbf{a}} = \bar{\mathbf{a}}(\mathbf{x})$, is obtained as the principal eigenvector of the diffusion tensor computed from diffusion-weighted MRI (see [14, 42]). The construction of $\bar{\mathbf{a}}$ and choice of diffusion constants is discussed in Section 5.

If the kinetic rate constants are all assumed constant, then there are two spatially-homogeneous equilibria, namely:

$$\begin{aligned} \text{healthy:} \quad & u \equiv k_0/k_1, \quad \tilde{u} \equiv 0, \\ \text{pathogenic:} \quad & u \equiv \tilde{k}_1/k_{12}, \quad \tilde{u} \equiv k_0/\tilde{k}_1 - k_1/k_{12}. \end{aligned} \quad (3)$$

Crucially, the pathogenic equilibrium is positive, and therefore physically relevant, if and only if the dimensionless *basic reproduction number* $R_0 := k_0 k_{12} / k_1 \tilde{k}_1$ is greater than unity. Indeed, as R_0 increases through unity, a transcritical bifurcation occurs: when $R_0 < 1$, the healthy equilibrium is stable and no other (physical) equilibrium exists, and when $R_0 > 1$, the healthy equilibrium is unstable and the pathogenic equilibrium is stable.

Nondimensionalization

We scale the variables as follows, where tildes indicate the new dimensionless variables [1]:

$$u = \frac{k_0}{k_1} \hat{u}, \quad \tilde{u} = \frac{k_0}{\tilde{k}_1} \hat{u}, \quad t = \frac{1}{\tilde{k}_1} \hat{t}, \quad x = \sqrt{\frac{d_{\text{ext}}}{\tilde{k}_1}} \hat{x}.$$

Substitution into the system (1) and dropping the tildes for notational convenience, we obtain the following dimensionless system:

$$\begin{cases} \epsilon \frac{\partial u}{\partial t} = \nabla \cdot (\boldsymbol{\delta} \nabla u) - u - R_0 u \tilde{u} + 1 & \text{in } \Omega \times (0, T], \\ \frac{\partial \tilde{u}}{\partial t} = \nabla \cdot (\boldsymbol{\delta} \nabla \tilde{u}) - \tilde{u} + R_0 \tilde{u} u & \text{in } \Omega \times (0, T], \\ (\boldsymbol{\delta} \nabla u) \cdot \mathbf{n} = 0, \quad (\boldsymbol{\delta} \nabla \tilde{u}) \cdot \mathbf{n} = 0 & \text{on } \partial\Omega \times (0, T], \\ u(\mathbf{x}, 0) = u_0(\mathbf{x}), \quad \tilde{u}(\mathbf{x}, 0) = \tilde{u}_0(\mathbf{x}) & \text{in } \Omega, \end{cases} \quad (4)$$

where

$$\epsilon = \frac{\tilde{k}_1}{k_1}, \quad R_0 = \frac{k_0 k_{12}}{k_1 \tilde{k}_1}, \quad \boldsymbol{\delta} = \frac{\mathbf{D}}{d_{\text{ext}}},$$

and the initial data u_0 and \tilde{u}_0 have been suitably rescaled and nondimensionalized.

2.2 Multiple-network porous media model

For the perfusion model, our starting point is the multiple-network porous medium model proposed in [11], which is in turn inspired by [31, 30, 64].

We suppose there are three vascular networks, namely arterial, capillary, and venous, with corresponding pressure fields $p_A(\mathbf{x}, t)$, $p_C(\mathbf{x}, t)$, $p_V(\mathbf{x}, t)$. Because the protein concentrations u , \tilde{u} evolve on timescales of hours to days, whereas p_A , p_C , p_V adjust to permeability changes (e.g. due to vasoconstriction) within seconds, we assume that all pressures are quasi-static. Conservation of mass then yields the following elliptic system:

$$\begin{cases} -\nabla \cdot (\mathbf{K}_A \nabla p_A) + \beta_{AC}(p_A - p_C) = 0, & \text{in } \Omega, \\ -\nabla \cdot (\mathbf{K}_C \nabla p_C) - \beta_{AC}(p_A - p_C) + \beta_{CV}(p_C - p_V) = 0, & \text{in } \Omega, \\ -\nabla \cdot (\mathbf{K}_V \nabla p_V) - \beta_{CV}(p_C - p_V) = 0, & \text{in } \Omega. \end{cases} \quad (5)$$

where β_{AC} and β_{CV} are the arterial-to-capillary and capillary-to-venous transfer coefficients. Since the brain's capillary network is isotropic, we have assumed $\mathbf{K}_C = k_C \mathbf{I}$, and we will specify the arterial and venous permeability tensors \mathbf{K}_A and \mathbf{K}_V on a case-by-case basis in Sections 4 and 5.

Arteries spanning the pial surface of the cortex supply the brain with blood; similarly, blood is drained by the pial venous network. Accordingly, we prescribe Dirichlet boundary conditions for the arterial and venous blood pressures on the pial surface $\Gamma_{\text{Pial}} \subset \partial\Omega$, together with a zero-flux condition for the capillary compartment:

$$p_A = p^{\text{Arteries}}, \quad p_V = p^{\text{Veins}}, \quad \nabla p_C \cdot \mathbf{n}_\Omega = 0 \quad \text{on } \Gamma_{\text{Pial}}. \quad (6)$$

The remaining part of the boundary is the brain's ventricular surface, $\Gamma_{\text{Vent}} := \partial\Omega \setminus \Gamma_{\text{Pial}}$, where we prescribe zero-flux conditions:

$$\nabla p_A \cdot \mathbf{n}_\Omega = \nabla p_C \cdot \mathbf{n}_\Omega = \nabla p_V \cdot \mathbf{n}_\Omega = 0, \quad \text{on } \Gamma_{\text{Vent}}. \quad (7)$$

Nondimensionalization

We scale the pressure fields so as to map the interval $[p^{\text{Veins}}, p^{\text{Arteries}}]$ uniformly onto $[0, 1]$:

$$p_A = (p^{\text{Arteries}} - p^{\text{Veins}})\hat{p}_A + p^{\text{Veins}}, \quad p_C = (p^{\text{Arteries}} - p^{\text{Veins}})\hat{p}_C + p^{\text{Veins}}, \quad p_V = (p^{\text{Arteries}} - p^{\text{Veins}})\hat{p}_V + p^{\text{Veins}},$$

and time and space are scaled as in Section 2.1. Substitution into (5) and the boundary conditions and omission of the tildes yields the dimensionless boundary value problem:

$$\begin{cases} -\nabla \cdot (\boldsymbol{\sigma}_A \nabla p_A) + p_A - p_C = 0, & \text{in } \Omega, \\ -\nabla \cdot (\boldsymbol{\sigma}_C \nabla p_C) + p_C - p_A + B(p_C - p_V) = 0, & \text{in } \Omega, \\ -\nabla \cdot (\boldsymbol{\sigma}_V \nabla p_V) + B(p_V - p_C) = 0, & \text{in } \Omega \\ p_A = 1, \quad p_V = 0, & \text{on } \Gamma_{\text{Pial}}, \\ \nabla p_A \cdot \mathbf{n}_\Omega = \nabla p_V \cdot \mathbf{n}_\Omega = 0, & \text{on } \Gamma_{\text{Vent}}, \\ \nabla p_C \cdot \mathbf{n}_\Omega = 0, & \text{on } \partial\Omega, \end{cases} \quad (8)$$

where

$$\boldsymbol{\sigma}_A = \frac{\tilde{k}_1 \mathbf{K}_A}{d_{\text{ext}} \beta_{AC}}, \quad \sigma_C = \frac{\tilde{k}_1 k_C}{d_{\text{ext}} \beta_{AC}}, \quad \boldsymbol{\sigma}_V = \frac{\tilde{k}_1 \mathbf{K}_V}{d_{\text{ext}} \beta_{AC}}, \quad B = \frac{\beta_{CV}}{\beta_{AC}}.$$

2.3 Coupled A β and perfusion model

In order to model the interaction between A β and the brain's microvasculature, we couple the protein and perfusion models of Sections 2.1 and 2.2, respectively. The biological mechanisms modeled here are reviewed in [36].

First, A β is vasoconstrictive, i.e. it induces blood vessels to become narrow [62, 45], thus increasing vascular resistance. In particular, Nortley et al. recently found that A β oligomers cause brain capillaries to constrict within seconds, through a mechanism involving oxidative stress and the vasoconstrictor endothelin 1 [46]. Therefore, we assume that the permeability of the capillary bed, k_C , is a decreasing sigmoidal function of the pathogenic protein concentration \tilde{u} :

$$\tilde{k}_C(\tilde{u}) = k_C - \left(k_C - k_C^{A\beta} \right) \tanh(\alpha_{k_C} \tilde{u}), \quad (9)$$

where k_C is the base permeability (in the absence of pathogenic proteins), $k_C^{A\beta}$ is the permeability for very large \tilde{u} , and α_{k_C} modulates the sensitivity to \tilde{u} . At the same time, we adopt a similar strategy for the transfer coefficients β_{AC} and β_{CV} . In particular, for a generic couple (i, j) , we define:

$$\tilde{\beta}_{ij}(\tilde{u}) = \beta_{ij} - \left(\beta_{ij} - \beta_{ij}^{A\beta} \right) \tanh(\alpha_{\beta_{ij}} \tilde{u}), \quad (10)$$

where $\alpha_{\beta_{ij}}$ is a constant that modulates the impact of misfolded A β on the flow between compartments. Indeed, according to the multiple-network porous medium theory developed in [2] for geophysical applications and later adapted for brain circulation in [64], the parameter β_{ij} models fluid exchange between networks. As discussed in [48], β_{ij} must be proportional to the exchange area between compartments. In Alzheimer's disease, A β induces capillary constriction [46], thus reducing capillary lumen and thus decreasing β_{AC} and β_{CV} . Through these couplings, pathogenic A β causes local decreases in permeability (i.e. increases in resistance), which we expect to cause hypoperfusion (reduced blood flow).

Conversely, hypoperfusion increases the production rate of A β [58, 60, 68]; it may also decrease its clearance rate [36], though this is less certain. Therefore, we let the rates of A β production and clearance depend on the rate of blood flow, as follows. We define the "CBF rate" at a point $\mathbf{x} \in \Omega$ as the rate of flow from the arterial compartment into the capillary bed per unit mass of tissue:

$$Q(p_A(\mathbf{x}), p_C(\mathbf{x})) = \frac{\beta_{AC}}{\rho} (p_A(\mathbf{x}) - p_C(\mathbf{x})), \quad (11)$$

where ρ is the brain tissue density estimated 1000 kg m^{-3} [29]. In particular, we denote by $Q_H = Q_H(\mathbf{x})$ the healthy CBF rate, i.e. corresponding to the pressure fields p_A , p_C when pathogenic proteins are absent (so that there is no

vasoconstriction). We now assume that the A β production rate increases in response to hypoperfusion, which we define as the relative decrease in Q from its healthy rate Q_H :

$$k_0^B(p_A, p_C) = k_0 + \kappa_0 \left(\frac{Q_H - Q(p_A, p_C)}{Q_H} \right), \quad (12)$$

where k_0 is the base rate, and κ_0 is the sensitivity to hypoperfusion. Similarly, we assume the clearance rates decrease in response to hypoperfusion:

$$k_1^B(p_A, p_C) = k_1 - \kappa_1 \left(\frac{Q_H - Q(p_A, p_C)}{Q_H} \right), \quad \tilde{k}_1^B(p_A, p_C) = \tilde{k}_1 - \tilde{\kappa}_1 \left(\frac{Q_H - Q(p_A, p_C)}{Q_H} \right). \quad (13)$$

The coupled protein–perfusion model is a parabolic–elliptic initial–boundary value problem to be solved for the concentrations $u(\mathbf{x}, t)$, $\tilde{u}(\mathbf{x}, t)$ and the pressures $p_A(\mathbf{x}, t)$, $p_C(\mathbf{x}, t)$, $p_V(\mathbf{x}, t)$:

$$\left\{ \begin{array}{ll} -\nabla \cdot (\mathbf{K}_A \nabla p_A) + \tilde{\beta}_{AC}(\tilde{u})(p_A - p_C) = 0 & \text{in } \Omega \times (0, T], \\ -\nabla \cdot (\tilde{k}_C(\tilde{u}) \nabla p_C) - \tilde{\beta}_{AC}(\tilde{u})(p_A - p_C) + \tilde{\beta}_{CV}(\tilde{u})(p_C - p_V) = 0 & \text{in } \Omega \times (0, T], \\ -\nabla \cdot (\mathbf{K}_V \nabla p_V) - \tilde{\beta}_{CV}(\tilde{u})(p_C - p_V) = 0 & \text{in } \Omega \times (0, T], \\ \frac{\partial u}{\partial t} = \nabla \cdot (\mathbf{D} \nabla u) - k_1^B(p_A, p_C) u - k_{12} u \tilde{u} + k_0^B(p_A, p_C) & \text{in } \Omega \times (0, T], \\ \frac{\partial \tilde{u}}{\partial t} = \nabla \cdot (\mathbf{D} \nabla \tilde{u}) - \tilde{k}_1^B(p_A, p_C) \tilde{u} + k_{12} \tilde{u} u & \text{in } \Omega \times (0, T], \\ \nabla p_A \cdot \mathbf{n} = \nabla p_V \cdot \mathbf{n} = 0, & \text{on } \Gamma_{\text{Vent}} \times (0, T], \\ \nabla p_C \cdot \mathbf{n} = 0, & \text{on } \partial\Omega \times (0, T], \\ p_A = p^{\text{Arteries}}, \quad p_V = p^{\text{Veins}}, & \text{on } \Gamma_{\text{Pial}} \times (0, T], \\ (\mathbf{D} \nabla u) \cdot \mathbf{n} = 0, \quad (\mathbf{D} \nabla \tilde{u}) \cdot \mathbf{n} = 0 & \text{on } \partial\Omega \times (0, T], \\ u(0, \mathbf{x}) = u_0(\mathbf{x}), \quad \tilde{u}(0, \mathbf{x}) = \tilde{u}_0(\mathbf{x}) & \text{in } \Omega. \end{array} \right. \quad (14)$$

Nondimensionalization

Rescaling as in previous sections, we obtain the dimensionless system:

$$\left\{ \begin{array}{ll} -\nabla \cdot (\boldsymbol{\sigma}_A \nabla p_A) + \tilde{\gamma}_{AC}(\tilde{u})(p_A - p_C) = 0 & \text{in } \Omega \times (0, T], \\ -\nabla \cdot (\tilde{\sigma}_C(\tilde{u}) \nabla p_C) - \tilde{\gamma}_{AC}(\tilde{u})(p_A - p_C) + B \tilde{\gamma}_{CV}(\tilde{u})(p_C - p_V) = 0 & \text{in } \Omega \times (0, T], \\ -\nabla \cdot (\boldsymbol{\sigma}_V \nabla p_V) - B \tilde{\gamma}_{CV}(\tilde{u})(p_C - p_V) = 0 & \text{in } \Omega \times (0, T], \\ \epsilon \frac{\partial u}{\partial t} = \nabla \cdot (\boldsymbol{\delta} \nabla u) - \lambda_1^B(p_A, p_C) u - R u \tilde{u} + \mu_0^B(p_A, p_C) & \text{in } \Omega \times (0, T], \\ \frac{\partial \tilde{u}}{\partial t} = \nabla \cdot (\boldsymbol{\delta} \nabla \tilde{u}) - \tilde{\lambda}_1^B(p_A, p_C) \tilde{u} + R \tilde{u} u & \text{in } \Omega \times (0, T], \\ p_A = 1, \quad p_V = 0, & \text{on } \Gamma_{\text{Pial}} \times (0, T], \\ \nabla p_A \cdot \mathbf{n} = \nabla p_V \cdot \mathbf{n} = 0, & \text{on } \Gamma_{\text{Vent}} \times (0, T], \\ \nabla p_C \cdot \mathbf{n} = 0, & \text{on } \partial\Omega \times (0, T], \\ (\boldsymbol{\epsilon} \boldsymbol{\delta} \nabla u) \cdot \mathbf{n} = 0, \quad (\boldsymbol{\delta} \nabla \tilde{u}) \cdot \mathbf{n} = 0, & \text{on } \partial\Omega \times (0, T], \\ u(0, \mathbf{x}) = u_0(\mathbf{x}), \quad \tilde{u}(0, \mathbf{x}) = \tilde{u}_0(\mathbf{x}), & \text{in } \Omega, \end{array} \right. \quad (15)$$

where

$$\begin{aligned}\tilde{\sigma}_C(\tilde{u}) &= \frac{\tilde{k}_1 \tilde{k}_C(\tilde{u})}{d_{\text{ext}} \beta_{AC}}, & \tilde{\gamma}_{AC}(\tilde{u}) &= \frac{1}{\beta_{AC}} \tilde{\beta}_{AC}(\tilde{u}), & \tilde{\gamma}_{CV}(\tilde{u}) &= \frac{1}{\beta_{CV}} \tilde{\beta}_{CV}(\tilde{u}), \\ \lambda_1^B(p_A, p_C) &= \frac{1}{k_1} k_1^B(p_A, p_C), & \tilde{\lambda}_1^B(p_A, p_C) &= \frac{1}{\tilde{k}_1} \tilde{k}_1^B(p_A, p_C), & \mu_0^B(p_A, p_C) &= \frac{1}{k_0} k_0^B(p_A, p_C).\end{aligned}$$

2.4 Weak formulation

To introduce a numerical approximation to Equation (14), we recall its variational formulation. We define the following Sobolev spaces

$$\begin{aligned}V &= H^1(\Omega), \\ V_0 &= H_0^1(\Omega) = \{v \in H^1(\Omega) : v = 0 \text{ on } \Gamma_{\text{Pial}}\}, \\ V_A^D &= \{v \in H^1(\Omega) : v = \tilde{p}^{\text{Arteries}} \text{ on } \Gamma_{\text{Pial}}\}, \\ V_V^D &= \{v \in H^1(\Omega) : v = \tilde{p}^{\text{Veins}} \text{ on } \Gamma_{\text{Pial}}\}.\end{aligned}$$

We denote by $(\cdot, \cdot)_\Omega$ the standard $L^2(\Omega)$ inner product. Given $k \in \mathbb{N}$ and a Hilbert space H , we denote by $C^k([0, T]; H)$ the space of functions $v = v(\mathbf{x}, t)$ such that v is k -times continuously differentiable with respect to t and $v(\cdot, t) \in H$ for each $t \in [0, T]$.

The weak formulation of problem (14) is to find, for each $t \geq 0$, functions

$$(p_A(t), p_C(t), p_V(t), u(t), \tilde{u}(t)) \in V_A^D \times V \times V_V^D \times V \times V$$

that satisfy:

$$(\mathbf{K}_A \nabla p_A, \nabla q_A)_\Omega + \left(\tilde{\beta}_{AC}(\tilde{u})(p_A - p_C), q_A \right)_\Omega = 0, \quad \forall q_A \in V_0, \quad (16a)$$

$$(\tilde{k}_C(\tilde{u}) \nabla p_C, \nabla q_C)_\Omega - \left(\tilde{\beta}_{AC}(\tilde{u})(p_A - p_C), q_C \right)_\Omega + \left(\tilde{\beta}_{CV}(\tilde{u})(p_C - p_V), q_C \right)_\Omega = 0, \quad \forall q_C \in V, \quad (16b)$$

$$(\mathbf{K}_V \nabla p_V, \nabla q_V)_\Omega - \left(\tilde{\beta}_{CV}(\tilde{u})(p_C - p_V), q_V \right)_\Omega = 0, \quad \forall q_V \in V_0, \quad (16c)$$

$$(\dot{u}, v)_\Omega + (\mathbf{D} \nabla u, \nabla v)_\Omega + (k_1^B(p_A, p_C) u, v)_\Omega + (k_{12} \tilde{u} u, v)_\Omega = (k_0^B(p_A, p_C), v)_\Omega, \quad \forall v \in V, \quad (16d)$$

$$(\dot{\tilde{u}}, \tilde{v})_\Omega + (\mathbf{D} \nabla \tilde{u}, \nabla \tilde{v})_\Omega + \left(\tilde{k}_1^B(p_A, p_C) \tilde{u}, \tilde{v} \right)_\Omega - (k_{12} u \tilde{u}, \tilde{v})_\Omega = 0, \quad \forall \tilde{v} \in V, \quad (16e)$$

$$u(0, \mathbf{x}) = u_0(\mathbf{x}), \quad \tilde{u}(0, \mathbf{x}) = \tilde{u}_0(\mathbf{x}), \quad \text{in } \Omega, \quad (16f)$$

where $\dot{\bullet} = \frac{\partial \bullet}{\partial t}$.

3 Discrete formulation

In this section, we introduce the discretization scheme for the resolution of the system in equation (16). In particular, in Section 3.1, we discuss the discretization in space, by means of a dG (discontinuous Galerkin) method, and in Section 3.2, we discretize in time by means of an implicit Euler time stepping algorithm.

3.1 Space discretization: discontinuous Galerkin method

First of all, let us introduce a mesh partition \mathcal{T}_h of the domain Ω made of simplicial elements K such that:

$$\forall K_i, K_j \in \mathcal{T}_h \quad |K_i \cap K_j| = 0 \quad \text{if} \quad i \neq j, \quad \text{and} \quad \bigcup_j K_j = \Omega,$$

where, for each element $K \in \mathcal{T}_h$, we denote by $|K|$ the measure of the element and by h_K its diameter. Moreover, we define $h := \max_{K \in \mathcal{T}_h} \{h_K\}$. If two elements share a common face F (e.g. the triangular interface of two tetrahedra), we call it an interior face, $F \in \mathcal{F}_h^I$. Otherwise, we call F a boundary face, $F \in \mathcal{F}_h^B$. We also partition the boundary faces into those on the pial and ventricular parts of $\partial\Omega$, i.e. $\mathcal{F}_h^B = \mathcal{F}_h^{\text{B, Vent}} \cup \mathcal{F}_h^{\text{B, Pial}}$. We denote by \mathcal{F}_h the set of all faces.

Let us now introduce the so-called trace operators. Let $F \in \mathcal{F}_h^I$ be a face shared by two elements K^\pm . We denote by \mathbf{n}^\pm the unit normal to F pointing out of K^\pm , respectively (see [51, Fig 11.1]). Then, for sufficiently regular scalar-valued functions q and vector-valued functions \mathbf{v} , we define the following operators:

- Average operator $\{\cdot\}$ on $F \in \mathcal{F}_h^I$ such that $\{q\} = \frac{1}{2}(q^+ + q^-)$, and $\{\mathbf{v}\} = \frac{1}{2}(\mathbf{v}^+ + \mathbf{v}^-)$.
- Jump operator $[\cdot]$ on $F \in \mathcal{F}_h^I$ such that $[q] = q^+ \mathbf{n}^+ + q^- \mathbf{n}^-$, and $[\mathbf{v}] = \mathbf{v}^+ \cdot \mathbf{n}^+ + \mathbf{v}^- \cdot \mathbf{n}^-$.

The \pm superscripts denote the traces on the face F of the functions defined on K^\pm [51, § 11.1]. In the same way, we define analogous operators on the face $F \in \mathcal{F}_h^B$ of a cell $K \in \mathcal{T}_h$, where \mathbf{n} is the outward unit normal on $\partial\Omega$:

- Average operator $\{\cdot\}$ on $F \in \mathcal{F}_h^B$ such that $\{q\} = q$ and $\{\mathbf{v}\} = \mathbf{v}$,
- Jump operator $[\cdot]$ on $F \in \mathcal{F}_h^B$ associated with a Neumann boundary condition such that $[q] = q\mathbf{n}$ and $[\mathbf{v}] = \mathbf{v} \cdot \mathbf{n}$,
- Jump operator $[\cdot]$ on $F \in \mathcal{F}_h^B$, with Dirichlet boundary conditions g and \mathbf{g} , associated with q and \mathbf{v} , respectively, such that $[q] = (q - g)\mathbf{n}$, and $[\mathbf{v}] = (\mathbf{v} - \mathbf{g}) \cdot \mathbf{n}$.

Let us define $\mathbb{P}_\ell(K)$ as the space of polynomials of total degree $\ell \geq 1$ over a mesh element K . Then we can introduce the following definitions of dG finite element spaces:

$$V_h^{\text{dG}} = \{v \in L^2(\Omega) : v|_K \in \mathbb{P}_\ell(K) \quad \forall K \in \mathcal{T}_h\}, \quad (17)$$

From now on, we introduce also a shorthand notation for the integrals over the faces $\int_{\mathcal{F}} = \sum_{F \in \mathcal{F}} \int_F$. These definitions can be used to introduce the following bilinear forms:

$$\begin{aligned} \mathcal{A}_A(v, w) &= \int_{\Omega} \mathbf{K}_A \nabla_h v \cdot \nabla_h w + \int_{\mathcal{F}_h^I \cup \mathcal{F}_h^{B, \text{Pial}}} (\eta[v] \cdot [w] - \{\mathbf{K}_A \nabla v\} \cdot [w] - [v] \cdot \{\mathbf{K}_A \nabla w\}) \, d\sigma \quad \forall v, w \in V_h^{\text{dG}}, \\ \mathcal{A}_C(v, w; \tilde{u}) &= \int_{\Omega} k_c(\tilde{u}) \nabla_h v \cdot \nabla_h w + \int_{\mathcal{F}_h^I} (\eta(\tilde{u})[v] \cdot [w] - \{k_c(\tilde{u}) \nabla v\} \cdot [w] - [v] \cdot \{k_c(\tilde{u}) \nabla w\}) \, d\sigma \quad \forall v, w \in V_h^{\text{dG}}, \\ \mathcal{A}_V(v, w) &= \int_{\Omega} \mathbf{K}_V \nabla_h v \cdot \nabla_h w + \int_{\mathcal{F}_h^I \cup \mathcal{F}_h^{B, \text{Pial}}} (\eta[v] \cdot [w] - \{\mathbf{K}_V \nabla v\} \cdot [w] - [v] \cdot \{\mathbf{K}_V \nabla w\}) \, d\sigma \quad \forall v, w \in V_h^{\text{dG}}, \\ \mathcal{A}_H(v, w) &= \int_{\Omega} \mathbf{D} \nabla_h v \cdot \nabla_h w + \int_{\mathcal{F}_h^I} (\eta[v] \cdot [w] - \{\mathbf{D} \nabla v\} \cdot [w] - [v] \cdot \{\mathbf{D} \nabla w\}) \, d\sigma \quad \forall v, w \in V_h^{\text{dG}}, \end{aligned}$$

The semi-discrete formulation in space reads as follows. Given the initial conditions $u_h(0) = u_{0h}$ and $\tilde{u}_h(0) = \tilde{u}_{0h}$, for each $t \in (0, T)$, find $(p_{Ah}(t), p_{Ch}(t), p_{Vh}(t), u_h(t), \tilde{u}_h(t)) \in (V_h^{\text{dG}})^5$ such that:

$$\mathcal{A}_A(p_{Ah}, q_{Ah}) + (\tilde{\beta}_{AC}(\tilde{u}_h)(p_{Ah} - p_{Ch}), q_{Ah})_{\Omega} = 0, \quad \forall q_A \in V_h^{\text{dG}}, \quad (18a)$$

$$\mathcal{A}_C(p_{Ch}, q_{Ch}; \tilde{u}_h) - (\tilde{\beta}_{AC}(\tilde{u}_h)(p_{Ah} - p_{Ch}), q_{Ch})_{\Omega} + (\tilde{\beta}_{CV}(\tilde{u}_h)(p_{Ch} - p_{Vh}), q_{Ch})_{\Omega} = 0, \quad \forall q_C \in V_h^{\text{dG}}, \quad (18b)$$

$$\mathcal{A}_V(p_{Vh}, q_{Vh}) - (\tilde{\beta}_{CV}(\tilde{u}_h)(p_{Ch} - p_{Vh}), q_{Vh})_{\Omega} = 0, \quad \forall q_V \in V_h^{\text{dG}}, \quad (18c)$$

$$(\dot{u}_h, v_h)_{\Omega} + \mathcal{A}_H(u_h, v_h) + (k_1^B(p_{Ah}, p_{Ch})u_h, v_h)_{\Omega} + (k_{12}\tilde{u}_h u_h, v_h)_{\Omega} - (k_0^B(p_{Ah}, p_{Ch}), v_h)_{\Omega} = 0 \quad \forall v \in V_h^{\text{dG}}, \quad (18d)$$

$$(\dot{\tilde{u}}_h, \tilde{v}_h)_{\Omega} + \mathcal{A}_H(\tilde{u}_h, \tilde{v}_h) + (\tilde{k}_1^B(p_{Ah}, p_{Ch})\tilde{u}_h, \tilde{v}_h)_{\Omega} - (k_{12}u_h \tilde{u}_h, \tilde{v}_h)_{\Omega} = 0, \quad \forall \tilde{v} \in V_h^{\text{dG}}. \quad (18e)$$

Algebraic formulation

Let $\{\varphi_j\}_{j=1}^N$ be suitable basis functions for the discrete spaces V_h^{dG} . Then we can write the unknowns as an expansion in the polynomial basis:

$$u_h(\mathbf{x}, t) = \sum_{j=1}^N U_n(t) \varphi_j(\mathbf{x}), \quad \tilde{u}_h(\mathbf{x}, t) = \sum_{j=1}^N \tilde{U}_n(t) \varphi_j(\mathbf{x}), \quad p_{kh}(\mathbf{x}, t) = \sum_{j=1}^{N_u} P_{kn}(t) \varphi_j(\mathbf{x}), \quad k = \{A, C, V\}.$$

We denote by $\mathbf{U} := [U_n]_{n=1}^N \in \mathbb{R}^N$, $\tilde{\mathbf{U}} := [\tilde{U}_n]_{n=1}^N \in \mathbb{R}^N$, $\mathbf{P}_k := [P_{kn}]_{n=1}^N \in \mathbb{R}^N$ the vectors of the expansion coefficients, and define the following matrices for $i, j = 1, \dots, N$:

$$[\mathbf{A}_A]_{ij} = \mathcal{A}_A(\varphi_j, \varphi_i) \quad (\text{Arterial stiffness matrix}); \quad (19a)$$

$$[\mathbf{A}_C(\tilde{\mathbf{U}}_h)]_{ij} = \mathcal{A}_C(\varphi_j, \varphi_i; \tilde{u}_h) \quad (\text{Capillary stiffness matrix}); \quad (19b)$$

$$[\mathbf{A}_V]_{ij} = \mathcal{A}_V(\varphi_j, \varphi_i) \quad (\text{Venous stiffness matrix}); \quad (19c)$$

$$[\mathbf{M}_{\beta_{AC}}(\tilde{\mathbf{U}}_h)]_{ij} = (\tilde{\beta}_{AC}(\tilde{u}_h)\varphi_j, \varphi_i)_\Omega \quad (\text{Arterial-capillary coupling matrix}); \quad (19d)$$

$$[\mathbf{M}_{\beta_{CV}}(\tilde{\mathbf{U}}_h)]_{ij} = (\tilde{\beta}_{CV}(\tilde{u}_h)\varphi_j, \varphi_i)_\Omega \quad (\text{Capillary-venous coupling matrix}); \quad (19e)$$

$$[\mathbf{M}]_{ij} = (\varphi_j, \varphi_i)_\Omega \quad (\text{Mass matrix}); \quad (19f)$$

$$[\mathbf{A}_H]_{ij} = \mathcal{A}_H(\varphi_j, \varphi_i) \quad (\text{Heterodimer stiffness matrix}); \quad (19g)$$

$$[\mathbf{M}_{k_1}(\mathbf{P}_{Ah}, \mathbf{P}_{Ch})]_{ij} = (k_1^B(p_{Ah}, p_{Ch})\varphi_j, \varphi_i)_\Omega \quad (\text{Healthy protein clearance matrix}); \quad (19h)$$

$$[\mathbf{M}_{\tilde{k}_1}(\mathbf{P}_{Ah}, \mathbf{P}_{Ch})]_{ij} = (\tilde{k}_1^B(p_{Ah}, p_{Ch})\varphi_j, \varphi_i)_\Omega \quad (\text{Misfolded protein clearance matrix}); \quad (19i)$$

$$[\mathbf{M}_{k_{12}}(\mathbf{V}_h)]_{ij} = (k_{12}v_h\varphi_j, \varphi_i)_\Omega \quad (\text{Protein misfolding matrix}). \quad (19j)$$

Moreover we define the forcing term $\mathbf{F}_{k_0}(\mathbf{P}_{Ah}, \mathbf{P}_{Ch}) = [(k_0^B(p_{Ah}, p_{Ch}), \varphi_j)_\Omega]_{j=1}^N$. The algebraic form of (18) can be written as: given $\mathbf{U}_h(0) = \mathbf{U}_{h,0}$ and $\tilde{\mathbf{U}}_h(0) = \tilde{\mathbf{U}}_{h,0}$, find $(\mathbf{P}_{Ah}(t), \mathbf{P}_{Ch}(t), \mathbf{P}_{Vh}(t), \mathbf{U}_h(t), \tilde{\mathbf{U}}_h(t)) \in \mathbb{R}^{5N}$ such that $\forall t \in (0, T]$ we have:

$$\mathbf{A}_A \mathbf{P}_{Ah} + \mathbf{M}_{\beta_{AC}}(\tilde{\mathbf{U}}_h) (\mathbf{P}_{Ah} - \mathbf{P}_{Ch}) = \mathbf{0}, \quad (20a)$$

$$\mathbf{A}_C(\tilde{\mathbf{U}}_h) \mathbf{P}_{Ch} - \mathbf{M}_{\beta_{AC}}(\tilde{\mathbf{U}}_h) (\mathbf{P}_{Ah} - \mathbf{P}_{Ch}) + \mathbf{M}_{\beta_{CV}}(\tilde{\mathbf{U}}_h) (\mathbf{P}_{Ch} - \mathbf{P}_{Vh}) = \mathbf{0}, \quad (20b)$$

$$\mathbf{A}_V \mathbf{P}_{Vh} - \mathbf{M}_{\beta_{CV}}(\tilde{\mathbf{U}}_h) (\mathbf{P}_{Ch} - \mathbf{P}_{Vh}) = \mathbf{0}, \quad (20c)$$

$$\mathbf{M} \dot{\mathbf{U}}_h + \mathbf{A}_H \mathbf{U}_h + \mathbf{M}_{k_1}(\mathbf{P}_{Ah}, \mathbf{P}_{Ch}) \mathbf{U}_h + \mathbf{M}_{k_{12}}(\tilde{\mathbf{U}}_h) \mathbf{U}_h = \mathbf{F}_{k_0}(\mathbf{P}_{Ah}, \mathbf{P}_{Ch}), \quad (20d)$$

$$\mathbf{M} \dot{\tilde{\mathbf{U}}}_h + \mathbf{A}_H \tilde{\mathbf{U}}_h + \mathbf{M}_{\tilde{k}_1}(\mathbf{P}_{Ah}, \mathbf{P}_{Ch}) \tilde{\mathbf{U}}_h - \mathbf{M}_{k_{12}}(\mathbf{U}_h) \tilde{\mathbf{U}}_h = \mathbf{0}. \quad (20e)$$

3.2 Time discretization: implicit Euler finite difference scheme

Finally, we must construct a fully discrete formulation, providing time discretization. For this purpose, we adopt an implicit Euler scheme to discretize the problem. We construct a time discretization of the interval $[0, T]$ by defining a partition of N intervals $0 = t_0 < t_1 < \dots < t_N = T$. We assume a constant timestep $\Delta t = t_{n+1} - t_n$, $n = 0, \dots, N-1$. Moreover, we split the resolution of the nonlinear problem into two steps, using a loosely-coupled scheme for the resolution of the porous media problem and the heterodimer one. Given \mathbf{U}_h^n and $\tilde{\mathbf{U}}_h^n$, solve

$$\mathbf{A}_A \mathbf{P}_{Ah}^{n+1} + \mathbf{M}_{\beta_{AC}}(\tilde{\mathbf{U}}_h^n) (\mathbf{P}_{Ah}^{n+1} - \mathbf{P}_{Ch}^{n+1}) = \mathbf{0}, \quad (21a)$$

$$\mathbf{A}_C(\tilde{\mathbf{U}}_h^n) \mathbf{P}_{Ch}^{n+1} - \mathbf{M}_{\beta_{AC}}(\tilde{\mathbf{U}}_h^n) (\mathbf{P}_{Ah}^{n+1} - \mathbf{P}_{Ch}^{n+1}) + \mathbf{M}_{\beta_{CV}}(\tilde{\mathbf{U}}_h^n) (\mathbf{P}_{Ch}^{n+1} - \mathbf{P}_{Vh}^{n+1}) = \mathbf{0}, \quad (21b)$$

$$\mathbf{A}_V \mathbf{P}_{Vh}^{n+1} - \mathbf{M}_{\beta_{CV}}(\tilde{\mathbf{U}}_h^n) (\mathbf{P}_{Ch}^{n+1} - \mathbf{P}_{Vh}^{n+1}) = \mathbf{0}, \quad (21c)$$

$$\left(\mathbf{M} + \Delta t \left(\mathbf{A}_H + \mathbf{M}_{k_1}(\mathbf{P}_{Ah}^{n+1}, \mathbf{P}_{Ch}^{n+1}) + \mathbf{M}_{k_{12}}(\tilde{\mathbf{U}}_h^n) \right) \right) \mathbf{U}_h^{n+1} = \mathbf{M} \mathbf{U}_h^n + \Delta t \mathbf{F}_{k_0}(\mathbf{P}_{Ah}^{n+1}, \mathbf{P}_{Ch}^{n+1}), \quad (21d)$$

$$\left(\mathbf{M} + \Delta t \left(\mathbf{A}_H + \mathbf{M}_{\tilde{k}_1}(\mathbf{P}_{Ah}^{n+1}, \mathbf{P}_{Ch}^{n+1}) - \mathbf{M}_{k_{12}}(\mathbf{U}_h^n) \right) \right) \tilde{\mathbf{U}}_h^{n+1} = \mathbf{M} \tilde{\mathbf{U}}_h^n. \quad (21e)$$

$$(21f)$$

In practice, first, we solve the porous media problem at time t^{n+1} by using the solution \tilde{u}_h^n

$$\begin{bmatrix} \mathbf{A}_A + \mathbf{M}_{\beta_{AC}}(\tilde{\mathbf{U}}_h^n) & -\mathbf{M}_{\beta_{AC}}(\tilde{\mathbf{U}}_h^n) & \mathbf{0} \\ -\mathbf{M}_{\beta_{AC}}(\tilde{\mathbf{U}}_h^n) & \mathbf{A}_C(\tilde{\mathbf{U}}_h^n) + \mathbf{M}_{\beta_{AC}}(\tilde{\mathbf{U}}_h^n) + \mathbf{M}_{\beta_{CV}}(\tilde{\mathbf{U}}_h^n) & -\mathbf{M}_{\beta_{CV}}(\tilde{\mathbf{U}}_h^n) \\ \mathbf{0} & -\mathbf{M}_{\beta_{CV}}(\tilde{\mathbf{U}}_h^n) & \mathbf{A}_V + \mathbf{M}_{\beta_{CV}}(\tilde{\mathbf{U}}_h^n) \end{bmatrix} \begin{bmatrix} \mathbf{P}_{Ah}^{n+1} \\ \mathbf{P}_{Ch}^{n+1} \\ \mathbf{P}_{Vh}^{n+1} \end{bmatrix} = \begin{bmatrix} \mathbf{0} \\ \mathbf{0} \\ \mathbf{0} \end{bmatrix}.$$

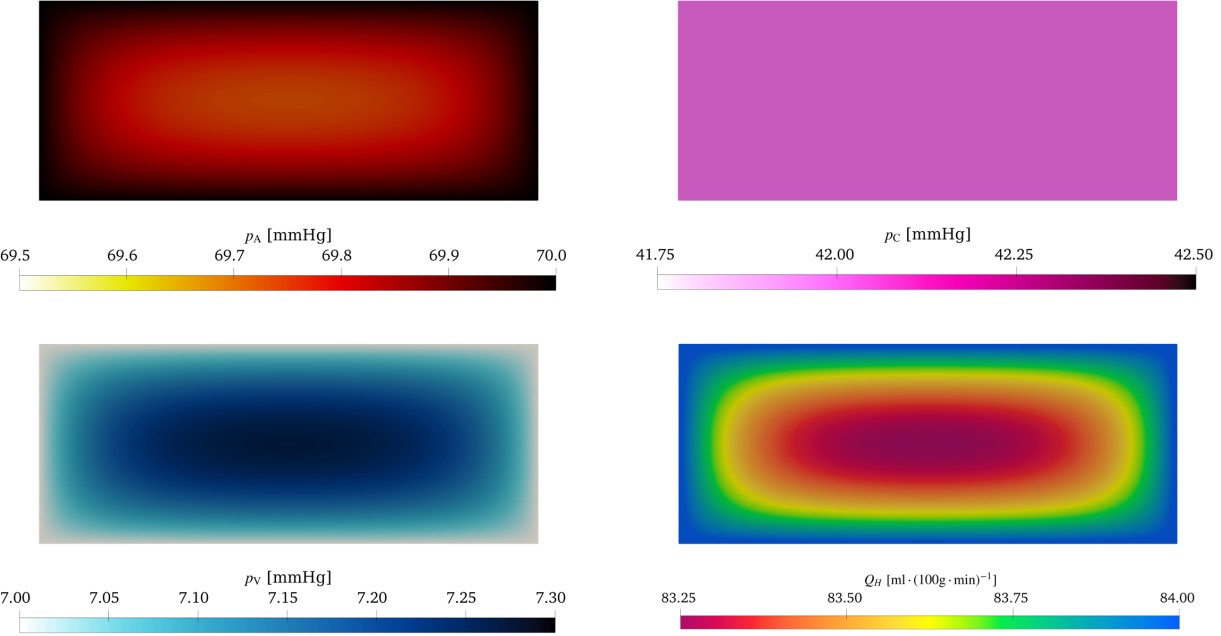


Figure 2: Test Case 1: Pressures computed in healthy conditions in the domain Ω . We report the arterial p_A (upper-left), capillary p_C (upper-right), and venous p_V (lower-left) pressures and the healthy CBF rate $Q_H = \frac{\beta_{AC}}{\rho}(p_A - p_C)$ (lower right).

Then, we solve the heterodimer model at the same time by using the pressures p_A^{n+1} and p_C^{n+1} with a decoupled strategy for the two variables (see [4])

$$\begin{aligned} \left(\mathbf{M} + \Delta t \left(\mathbf{A}_H + \mathbf{M}_{k_1}(\mathbf{P}_{Ah}^{n+1}, \mathbf{P}_{Ch}^{n+1}) + \mathbf{M}_{k_{12}}(\tilde{\mathbf{U}}_h^n) \right) \right) \mathbf{U}_h^n &= \mathbf{M}\mathbf{U}_h^n + \Delta t \mathbf{F}_{k_0}(\mathbf{P}_{Ah}^{n+1}, \mathbf{P}_{Ch}^{n+1}), \\ \left(\mathbf{M} + \Delta t \left(\mathbf{A}_H + \mathbf{M}_{\tilde{k}_1}(\mathbf{P}_{Ah}^{n+1}, \mathbf{P}_{Ch}^{n+1}) - \mathbf{M}_{k_{12}}(\mathbf{U}_h^n) \right) \right) \tilde{\mathbf{U}}_h^n &= \mathbf{M}\tilde{\mathbf{U}}_h^n. \end{aligned}$$

4 Numerical validation in simple geometries

We now present some simple test cases to highlight some properties of the model introduced in Equation (14). We consider an idealized rectangular domain $\Omega = (0 \text{ m}, 0.1 \text{ m}) \times (0 \text{ m}, 0.4 \text{ m})$ and a final time $T = 100$ years. We impose Dirichlet boundary conditions on $\partial\Omega$ for the pressures, representing constant arterial and venous blood pressures at the brain–body vascular interface. We use a structured triangular mesh with 15 000 elements, a polynomial degree $\ell = 1$ for all five discretized fields, and a time step of $\Delta t = 0.05$ years. Unless otherwise indicated, all spatial coordinates in this section represent values in metres (m).

4.1 Test Case 1: Multistability dependent on the initial condition

In this test case, we consider a rectangular domain and prescribe initial data with a localized region of high pathogenic protein concentration, called the “seeding region”. We are interested in whether all such “pathogenic seeds” trigger disease spread, as is the case for most reaction–diffusion models of A β in the literature [66, 20, 4, 10]. The parameter values used in this test case are given in Appendix A (Table 1).

We must first compute the healthy perfusion rate Q_H from Equation (5), which represents the healthy CBF rate in the absence of A β or other vascular pathologies. Figure 2 shows the numerical solution. The gradients in arterial and venous pressure near the boundary determine the flux into and out of the domain. The capillary pressure is spatially almost constant because the the value used for the permeability k_C (reported in Table 1 in Appendix A) is relatively large.

As initial data for the normal (u_0) and misfolded (\tilde{u}_0) protein concentrations, we first consider a seeding region

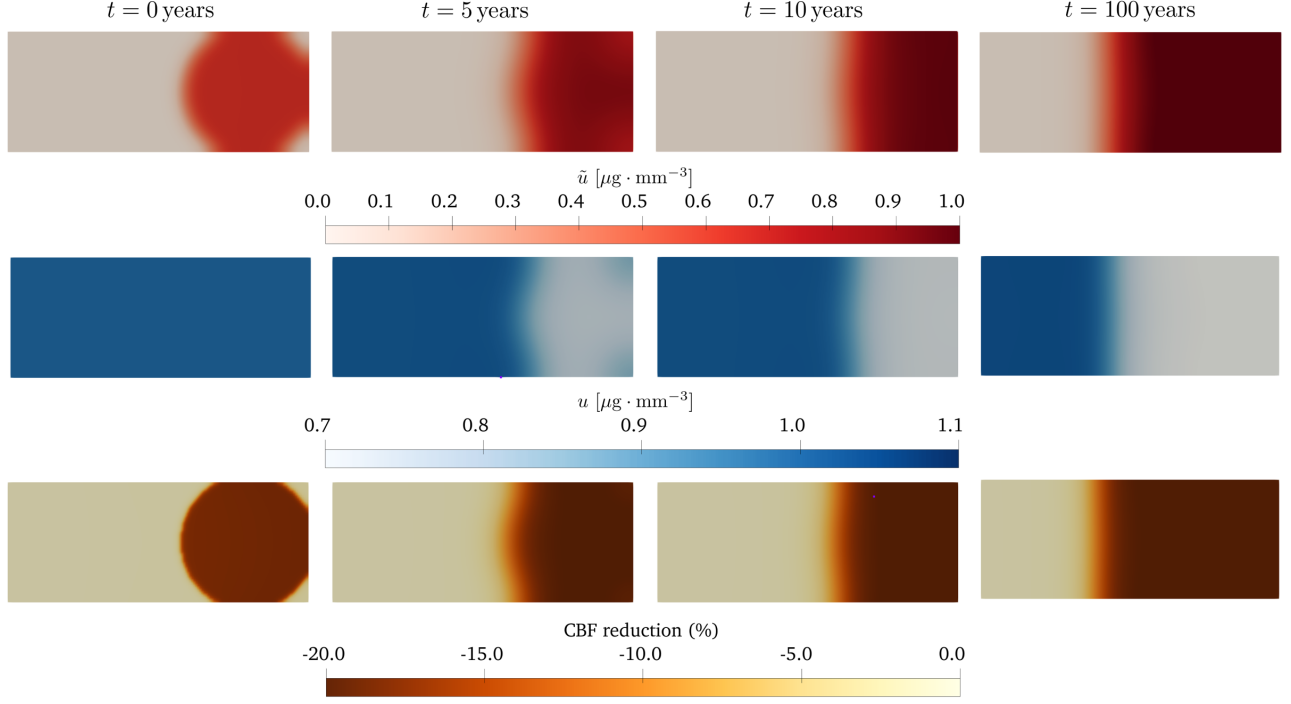


Figure 3: Numerical solution for Test Case 1 with large seeding region. Misfolded proteins \tilde{u} (first row), healthy proteins u (second row), and reduction of CBF (third row). Disease propagation *succeeds*.

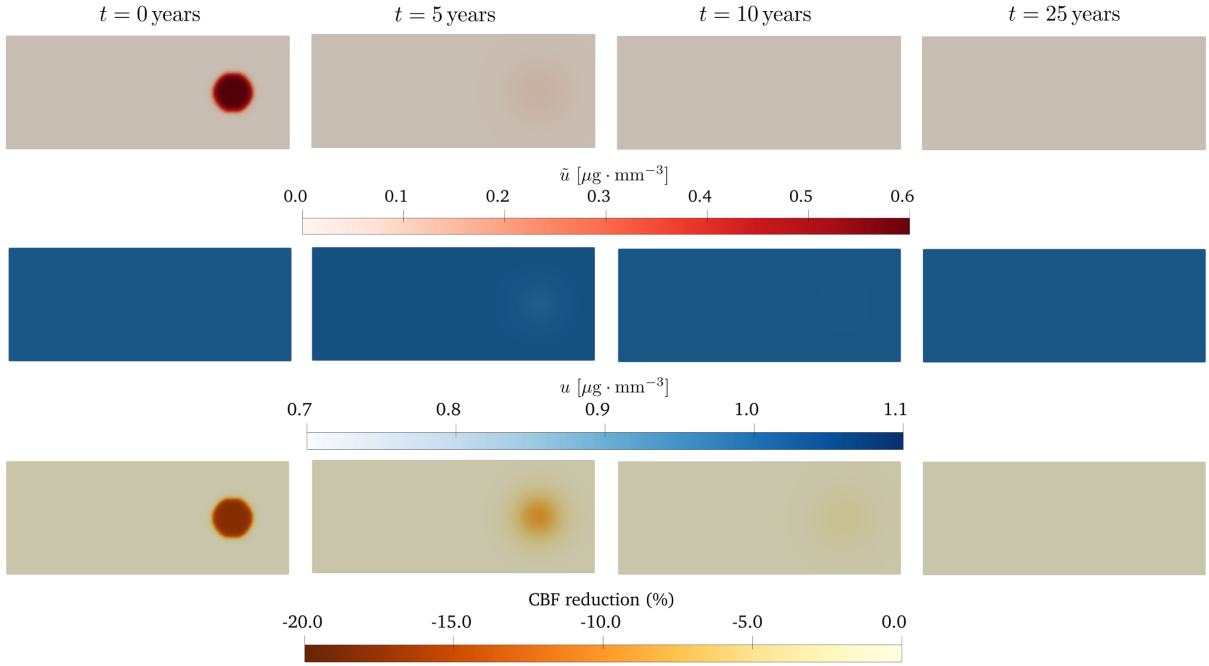


Figure 4: Numerical solution for Test Case 1 with small seeding region. Disease propagation *fails*.

with large radius (see Figure 3, $t = 0$):

$$\text{Large: } u_0(x, y) = 1.0 \mu\text{g} \cdot \text{mm}^{-3}, \quad \tilde{u}_0(x, y) = \begin{cases} 0.6 \mu\text{g} \cdot \text{mm}^{-3} & (x - 0.08)^2 + (y - 0.02)^2 < 5 \times 10^{-4}, \\ 0.0 \mu\text{g} \cdot \text{mm}^{-3} & \text{elsewhere.} \end{cases}$$

Figure 3 shows the simulation’s evolution: the pathogenic protein concentration increases and saturates locally, and spreads through space like a travelling wave. Behind the wave front, the system is in a diseased state, which invades the healthy region ahead of the wave front. The CBF rate exhibits a reduction of approximately 20% in the diseased region.

Next, we consider a seeding region with a smaller radius (see Figure 4, $t = 0$):

$$\text{Small: } u_0(x, y) = 1.0 \mu\text{g} \cdot \text{mm}^{-3}, \quad \tilde{u}_0(x, y) = \begin{cases} 0.6 \mu\text{g} \cdot \text{mm}^{-3} & (x - 0.08)^2 + (y - 0.02)^2 < 5 \times 10^{-5}, \\ 0.0 \mu\text{g} \cdot \text{mm}^{-3} & \text{elsewhere.} \end{cases}$$

In contrast to the previous case, the results in Figure 4 reveal that propagation *fails*, i.e. the initial pathogenic seed decays and the system returns to the healthy state.

This test case demonstrates that (1) the coupled model (14) has multiple stable equilibrium states, and (2) disease outbreak is dependent on the initial data. Specifically, if the initial seed of pathogenic proteins is sufficiently small (small concentration and/or small seeding region), then it decays back to the healthy equilibrium; but if the seed is large enough, then disease outbreak occurs locally and spreads like a wave through space. This behaviour is reminiscent of *bistable* reaction–diffusion systems (see [33]), and contrasts with most reaction–diffusion models of A β in the literature, which are *monostable* and exhibit disease spread for every $\tilde{u}_0 \not\equiv 0$.

4.2 Test Case 2: Injury-induced initiation of the pathology

The following test case is motivated by the two-hit vascular hypothesis of AD (see Section 1), which states that the initial cause of AD is vascular damage, which then triggers A β dyshomeostasis and disease spread [69, 53, 35]. We suppose that a vascular injury affects a localized region of space, $\Omega_{\text{inj}} \subset \Omega$, causing CBF to decrease. Focal ischaemia of this kind can arise from stroke (symptomatic or asymptomatic), small vessel disease (e.g. in a watershed region), or atherosclerosis of an upstream artery [23, 41, 59, 52].

We model the injury as a localized decrease in the transfer coefficients from the arterial to capillary compartments, representing a decrease in the supply of oxygenated arterial blood to the capillary bed. We also decrease the capillary to venous transfer coefficient and the capillary bed’s permeability to model the constriction of the capillaries typically induced by those injuries [52]:

$$\begin{aligned} \beta_{\text{AC}} &= \begin{cases} 4.25 \times 10^{-7} (\text{Pa} \cdot \text{s})^{-1} & \text{in } \Omega_{\text{inj}}, \\ 5.00 \times 10^{-7} (\text{Pa} \cdot \text{s})^{-1} & \text{in } \Omega \setminus \Omega_{\text{inj}}, \end{cases} & \beta_{\text{CV}} &= \begin{cases} 3.25 \times 10^{-7} (\text{Pa} \cdot \text{s})^{-1} & \text{in } \Omega_{\text{inj}}, \\ 4.00 \times 10^{-7} (\text{Pa} \cdot \text{s})^{-1} & \text{in } \Omega \setminus \Omega_{\text{inj}}, \end{cases} \\ k_{\text{C}} &= \begin{cases} 2.00 \times 10^{-7} (\text{Pa} \cdot \text{s})^{-1} & \text{in } \Omega_{\text{inj}}, \\ 5.00 \times 10^{-7} (\text{Pa} \cdot \text{s})^{-1} & \text{in } \Omega \setminus \Omega_{\text{inj}}. \end{cases} \end{aligned}$$

All other parameters are spatially homogeneous and are given in Appendix A (Table 1). The initial protein concentrations are given by:

$$u_0 \equiv 1.0 \mu\text{g} \cdot \text{mm}^{-3}, \quad \tilde{u}_0 \equiv 0.05 \mu\text{g} \cdot \text{mm}^{-3},$$

representing a small perturbation from the healthy equilibrium state. The healthy CBF rate field $Q_{\text{H}} = Q_{\text{H}}(\mathbf{x})$ is the same as in Test Case 1 (Figure 2).

We first consider an injury site with large radius:

$$\text{Large injury site: } \Omega_{\text{inj}} = \{(x, y) \in \Omega \mid (x - 0.05)^2 + (y - 0.02)^2 < 5 \times 10^{-4}\}$$

The simulation results are shown in Figure 5. The reductions in β_{AC} , β_{CV} and k_{C} inside Ω_{inj} cause a $\sim 16.5\%$ CBF rate decrease inside Ω_{inj} at $t = 0$. This injury-induced hypoperfusion triggers accumulation of misfolded proteins at the injury site, as seen in Figure 5, followed by disease spread from the injury site to the rest of space. We note that the initial increase in u within Ω_{inj} is caused by the hypoperfusion-induced increase in its production rate—see (12)—and decrease in its clearance rate; after some time, (u, \tilde{u}) switches to its diseased state behind the invading wave front, which explains the decrease in u from $t = 10$ on.

Next, we consider an injury site with a smaller radius:

$$\text{Small injury site: } \Omega_{\text{inj}} = \{(x, y) \in \Omega \mid (x - 0.05)^2 + (y - 0.02)^2 < 5 \times 10^{-5}\}$$

In this case, we observe from the simulation results in Figure 6 that the induced focal hypoperfusion is not sufficient to trigger disease outbreak, and the healthy state remains stable, in contrast to the case of the large injury site.

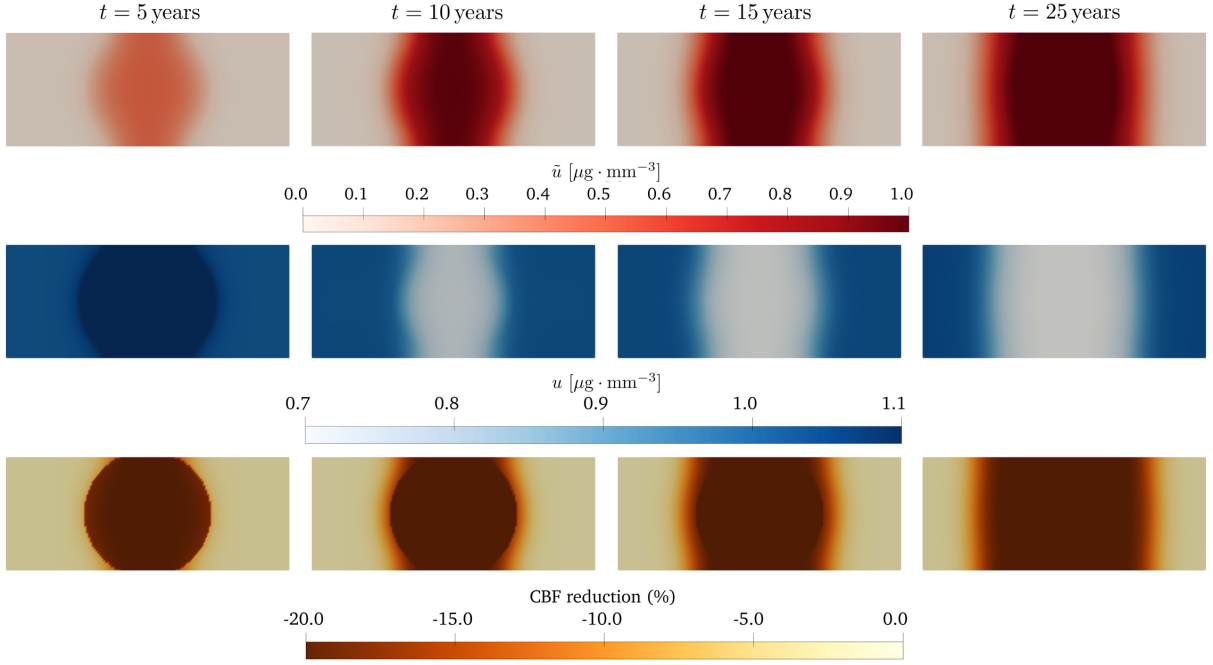


Figure 5: Numerical solution for Test Case 2 with large injury site. Localized injury triggers disease spread.

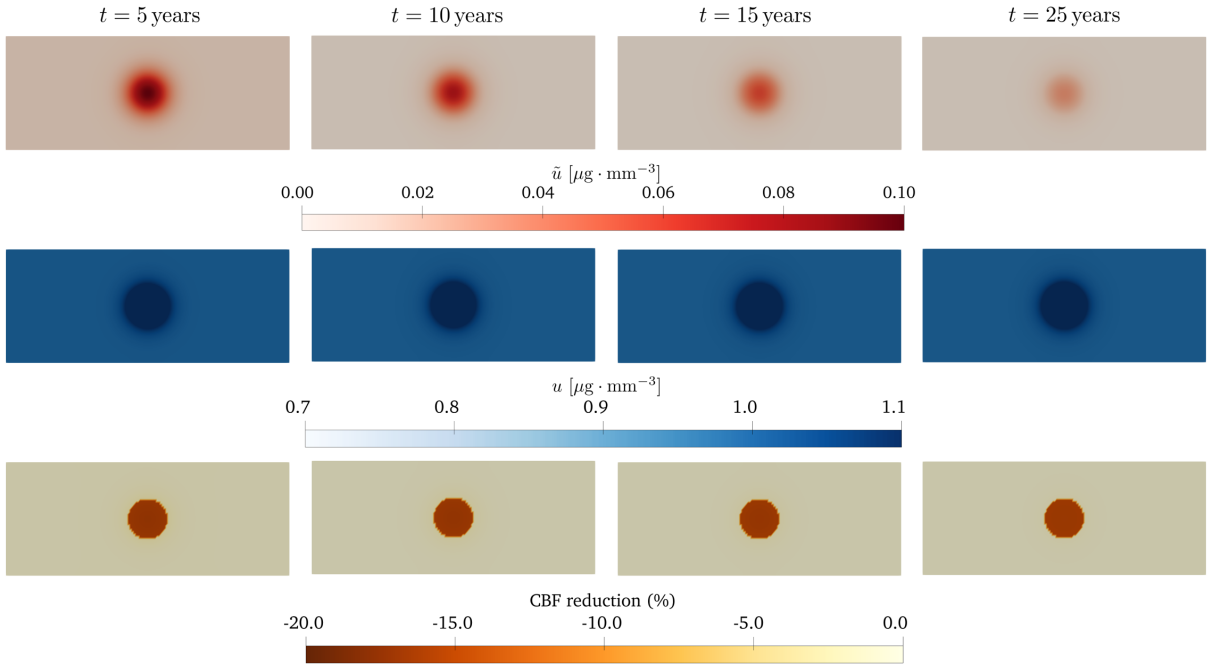


Figure 6: Numerical solution for Test Case 2 with small injury site. Injury is insufficient to trigger disease spread.

This test case is of considerable interest biologically and mathematically, as it represents the possibility of *locally-induced* global disease outbreak. The intuition is that localized hypoperfusion due to vascular injury, provided it is sufficiently severe, can trigger disease outbreak locally, thus creating a bridgehead from which to invade healthy tissue; see [1, §5], which introduced this idea.

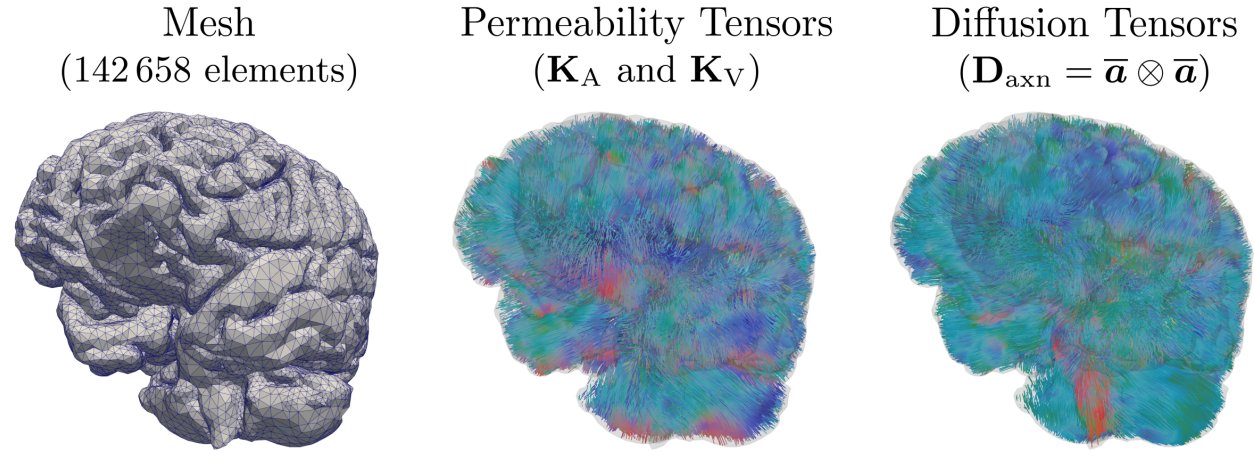


Figure 7: Tetrahedral mesh of the brain (left), directions of permeability tensors \mathbf{K}_A and \mathbf{K}_V (centre), and axonal directions of the diffusion tensor \mathbf{D}_{axn} (right). In the visualization of the permeability and axonal directions, blue indicates directions in the x -axis, green indicates directions in the y -axis, and red indicates directions in the z -axis.

5 Numerical simulations across the whole brain

We extend the two test cases from Section 4 to a realistic brain geometry. The goal is to demonstrate how the properties of the mathematical model in equation (14) enable simulation of realistic pathological scenarios. Starting from a structural MRI in the OASIS-3 database [37], we generate a brain segmentation using FreeSurfer [18]. We then construct a tetrahedral mesh with 142,658 elements (see Figure 7, left) using the SVMToolkit library [42].

For the simulation setup, we set a final time $T = 40$ years and time step $\Delta t = 0.05$ years. Polynomial degrees are $\ell = 1$ for pressures p_A , p_C , p_V and $\ell = 2$ for protein concentrations u and \tilde{u} . Physical parameters are listed in Appendix A, Table 2. Simulations were run on the GALILEO100 supercomputer (528 nodes, each with 2×Intel Cascade Lake 8260 CPUs, 24 cores, 2.4 GHz, 384 GB RAM) at the CINECA supercomputing center.

Construction of the permeability and diffusion tensors

To solve the perfusion porous-medium problem, we describe the perfusion tensors \mathbf{K}_A and \mathbf{K}_V for the arterioles and venules, respectively. Specifically, we follow the strategy proposed in [31] to derive directions approximately orthogonal to the pial surface, consistent with medical knowledge [55]. The resulting principal direction fibers $\bar{\mathbf{k}}(\mathbf{x})$, such that $\mathbf{K}_j = k_j(\bar{\mathbf{k}} \otimes \bar{\mathbf{k}})$ for $j = A, V$, are shown in Figure 7 (center).

We compute the axonal component of the diffusion tensor \mathbf{D}_{axn} from Diffusion Weighted Images (DWI) using FreeSurfer [18]. We then extract the principal eigenvector $\bar{\mathbf{a}}(\mathbf{x})$ to obtain the fiber directions, shown in Figure 7 (right).

Healthy CBF rate and pressures

As discussed in Section 4, to solve problem (14), we first solve (5) for the healthy CBF rate $Q_H = Q_H(\mathbf{x})$ (in the absence of pathogenic proteins). In all brain simulations, we impose Dirichlet boundary conditions for both arterial and venous pressures on the brain's pial surface Γ_{Pial} and homogeneous Neumann conditions on the ventricular surface Γ_{Vent} [11].

The solution is shown in Figure 8. The arterial pressure p_A reaches its maximum (~ 70 mmHg) at the pial surface. The peaks of the capillary and venous pressures p_C and p_V occur near the center of the domain, around the ventricular wall. These computed values agree with the literature [31]. We estimate the CBF rate inside the brain at $25\text{--}40 \text{ ml} \cdot \text{min}^{-1} \cdot (100 \text{ g})^{-1}$, consistent in magnitude with medical measurements, which show a decay in white matter relative to grey matter [17].

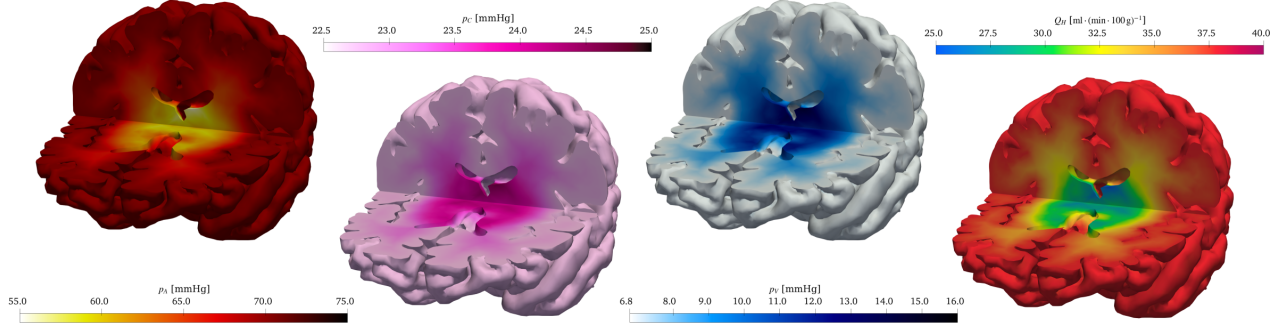


Figure 8: Pressures computed in healthy conditions in the brain. From left to right, we report the arterial p_A , capillary p_C , and venous p_V pressures and the healthy perfusion flow Q_H .

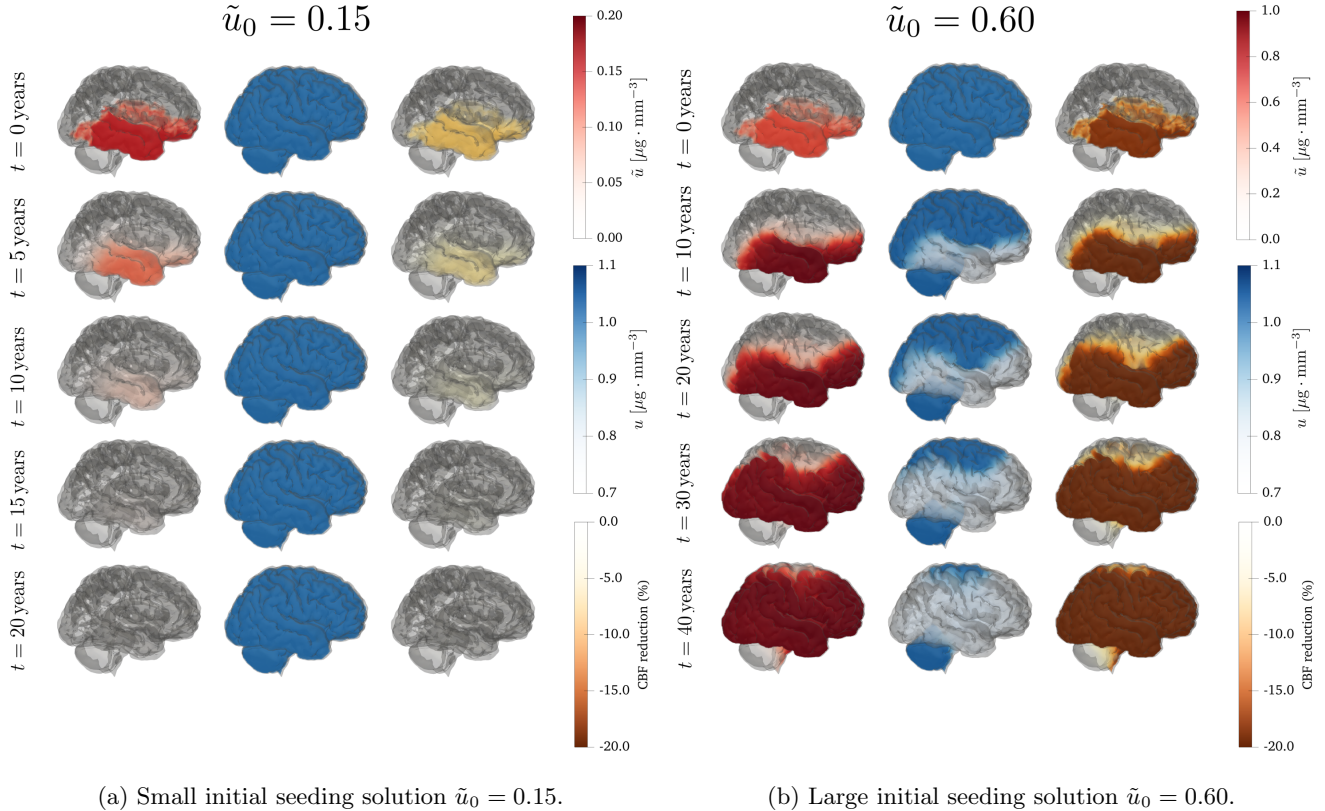


Figure 9: Test Case 3: Numerical solution comparing two different initial seeding magnitude: small seeding (a) and large seeding (b). In each panel, misfolded proteins \tilde{u} (first column), healthy proteins u (second column), and reduction of CBF (third column) are reported.

5.1 Test Case 3: Sensitivity to A β -seeding region

As in Test Case 1, we examine the impact of the initial pathogenic A β distribution on the model's dynamics. Depending on its magnitude, an initial pathogenic seed can grow and spread like a wave through space or it can decay completely. Here, we simulate two initial conditions, one large and one small, both located in the basal temporal and orbitofrontal neocortex, Ω_{seed} , typical regions for the first phase of amyloid progression [22].

First, we test a small localized concentration of misfolded protein ($\tilde{u}_0 = 0.15 \mu\text{g} \cdot \text{mm}^{-3}$ in Ω_{seed}) with constant healthy protein $u = 1 \mu\text{g} \cdot \text{mm}^{-3}$ throughout the domain. Figure 9a shows the result. Hypoperfusion in the temporal lobe—automatically induced by our initial condition—agrees with early AD literature [16]. The pathology does not

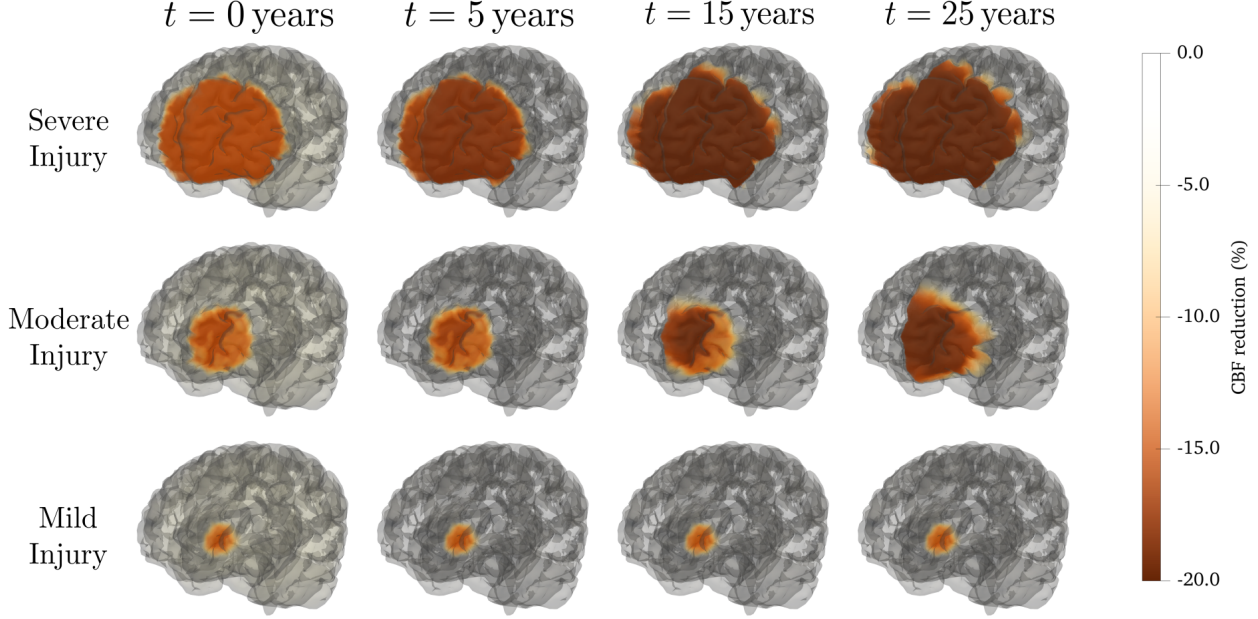


Figure 10: Test Case 4: Reduction of CBF at different times $t = 0, 5, 15, 25$ years and for three different dimensions of the hypoperfusion region: severe (first row), moderate (second row), and mild (third row).

develop: $\text{A}\beta$ concentration decays, restoring the neocortex to the healthy equilibrium.

Next, we increase the seeding magnitude to $\tilde{u}_0 = 0.60 \mu\text{g} \cdot \text{mm}^{-3}$ in Ω_{seed} . As shown in Figure 9b, this large initial seeding causes $\text{A}\beta$ spreading through the cortical area, with associated neocortical hypoperfusion. This rise in misfolded proteins coincides with a local decrease in healthy protein population. The computed CBF rate drops by $\sim 20\%$, consistent with the literature [36]. The spreading pattern first involves the temporal lobe [43], then diffuses to the upper cortex (occipital and frontal) [61], with the parietal lobe, brainstem, and cerebellum affected last—matching the stages in [22]. This reflects the spatial path length of the pathological wavefront.

These simulations extend Test Case 1 to a realistic scenario with clinical relevance. They demonstrate the model’s *multistability*, which implies that arbitrary pathogenic seeds *do not guarantee* disease accumulation and spread, in contrast to existing *monostable* models of $\text{A}\beta$ pathology [66, 20].

5.2 Test Case 4: Injury-induced initiation of $\text{A}\beta$ misfolding

As an extension of Test Case 2, we analyze the effect of an injured subdomain size $|\Omega_{\text{inj}}|$ on $\text{A}\beta$ misfolding and spreading through the brain. We adopt the physical parameters from Appendix A (Table 2), except for

$$\begin{aligned} \beta_{\text{AC}} &= \begin{cases} 8.50 \times 10^{-7} (\text{Pa} \cdot \text{s})^{-1} & \text{in } \Omega_{\text{inj}}, \\ 1.00 \times 10^{-6} (\text{Pa} \cdot \text{s})^{-1} & \text{in } \Omega \setminus \Omega_{\text{inj}}, \end{cases} & \beta_{\text{CV}} &= \begin{cases} 4.50 \times 10^{-7} (\text{Pa} \cdot \text{s})^{-1} & \text{in } \Omega_{\text{inj}}, \\ 3.00 \times 10^{-6} (\text{Pa} \cdot \text{s})^{-1} & \text{in } \Omega \setminus \Omega_{\text{inj}}, \end{cases} \\ k_{\text{C}} &= \begin{cases} 2.50 \times 10^{-13} (\text{Pa} \cdot \text{s})^{-1} & \text{in } \Omega_{\text{inj}}, \\ 4.28 \times 10^{-13} (\text{Pa} \cdot \text{s})^{-1} & \text{in } \Omega \setminus \Omega_{\text{inj}}, \end{cases} \end{aligned}$$

which induce injury in the frontal lobe of the left hemisphere. The hypoperfusion region is

$$\Omega_{\text{inj}} = \{(x, y, z) \in \Omega \mid (x - 0.01)^2 + (y - 0.08)^2 + (z - 0.015)^2 < \rho\},$$

with radii $\rho \in \{0.01, 0.02, 0.04\} \text{ m}$ for mild, moderate, and severe injuries, respectively. Initial conditions are constant: $u_0 = 1.0 \mu\text{g} \cdot \text{mm}^{-3}$ and $\tilde{u}_0 = 0.05 \mu\text{g} \cdot \text{mm}^{-3}$ for healthy and misfolded proteins, respectively—representing a small perturbation from the healthy equilibrium. In Figure 10, we observe that already at the initial time $t = 0$, the parameters induce a significant reduction of the CBF rate in the injured region (approximately 15%) in all cases.

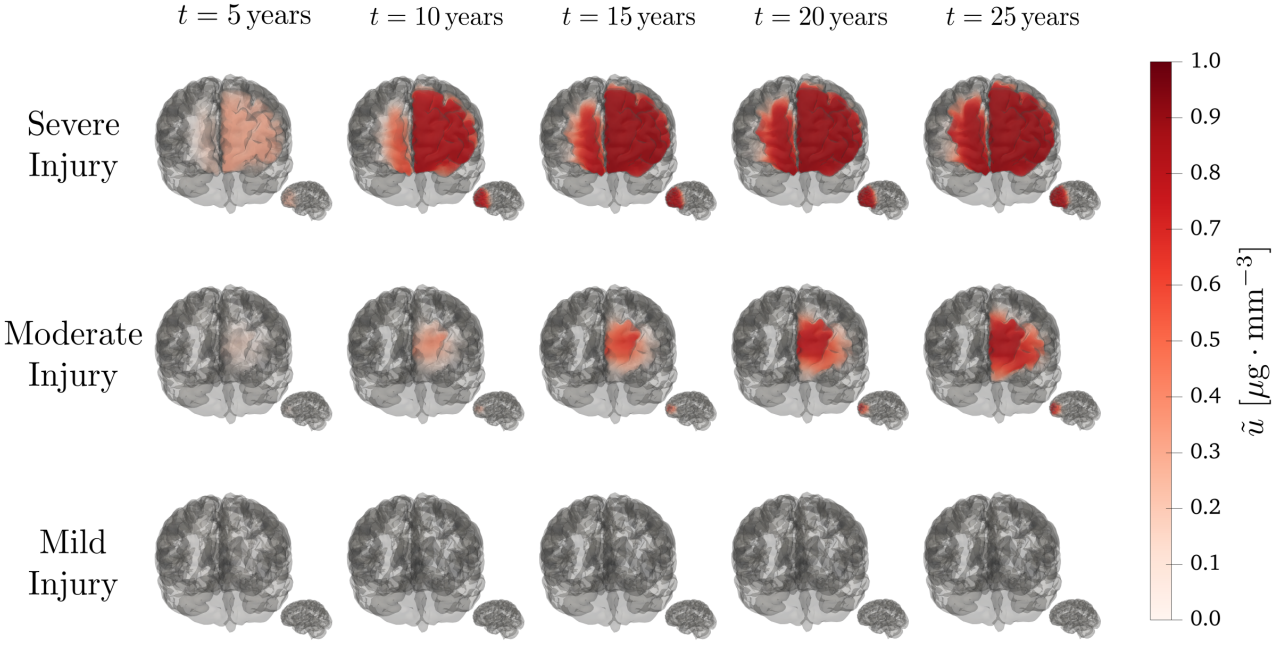


Figure 11: Test Case 4: Misfolded protein concentration u at different times $t = 5, 10, 15, 20, 25$ years and for three different dimensions of the hypoperfusion region: severe (first row), moderate (second row), and mild (third row).

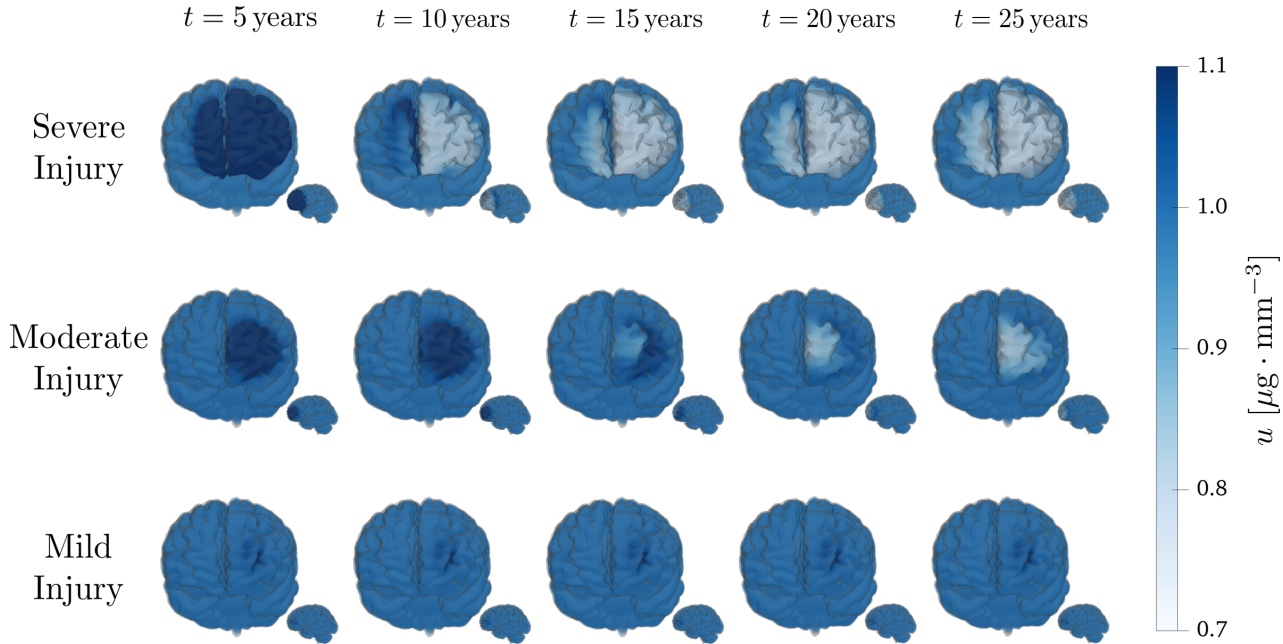


Figure 12: Test Case 4: Healthy protein concentration u at different times $t = 5, 10, 15, 20, 25$ years and for three different dimensions of the hypoperfusion region: severe (first row), moderate (second row), and mild (third row).

Figures 11 and 12 show the dynamics of misfolded and healthy protein concentrations, respectively. Moderate and severe injuries increase the pathogenic A β concentration (\tilde{u}) in the hypoperfused region, which then propagates through the frontal brain area—especially in the severe case. For the healthy A β concentration, we observe an initial concentration increase within the injured region, consistent with hypoperfusion-induced APP upregulation [25],

followed by a decrease in concentration as the injured region switches to the diseased equilibrium, for which $u < 1$. Figure 10 shows an expansion of the hypoperfused region outward from the initial injury site in the severe and moderate cases, caused by the pathogenic A β distribution which induces vasoconstriction as it spreads.

In the mild injury case, the pathogenic A β concentration decays nearly vanishes within 5 years, while healthy protein shows slight upregulation to mitigate neuronal injury [25] (see Figures 11 and 12). The initial hypoperfusion region remains unchanged.

These results mirror those in Test Case 2. They reveal that hypoperfusive injury, if sufficiently severe, may be capable of inducing the outbreak of mixed A β –vascular pathology *and* its spatial invasion of otherwise healthy brain regions. This model behavior aligns with prior modelling work [1].

6 Conclusion

Alzheimer’s disease, the most common cause of dementia, is characterized by the accumulation and spread of misfolded A β proteins in the brain, and is also associated with chronic cerebrovascular pathology [41]. The work presented here is motivated by the growing recognition of a positive feedback loop between A β accumulation and hypoperfusion in AD [26, 32, 36]. Our model describes the coupling between A β and cerebral blood flow (CBF) associated with A β -induced vasoconstriction [46, 62, 45] and hypoperfusion-induced modulation of A β metabolism [57, 58, 60, 68].

The model is similar in spirit to that of Ahern et al. [1], who assumed the same biological mechanisms. Whereas these authors used a network-based model of the brain and a semi-mechanistic model of blood flow within the network regions, the model presented here is continuous in space as well as in time, and its description of perfusion is based on multiple-network porous medium model. Interestingly, the emergent dynamics of the two models are qualitatively similar. Both exhibit multistability (Test Cases 1 and 3) and a capacity for vascular injury-induced disease outbreak (Test Cases 2 and 4), adding to the argument that these processes emerge generically.

From a numerical point of view, the differential equation has been discretized using a high-order discontinuous Galerkin method in space and implicit Euler time stepping in time. The model’s multistability was demonstrated for both idealized and realistic brain geometries. Moreover, we analyzed the possibility of describing the hypoperfusion-induction of the AD by introducing an initial hypoperfusion in the mathematical model. Finally, the numerical simulations on realistic brain geometries have been performed to highlight the importance of vascular–protein coupling in the mathematical description of AD pathology. Those simulations provided the typical spreading patterns of the pathology and confirmed the model quality in describing the physical phenomena.

A limitation of the present model concerns the adoption of the heterodimer model, which provides a simplified description of A β kinetics and axonal transport. Furthermore, all parameters were assumed to be constant, thus disregarding spatial heterogeneities in the underlying brain tissue. A possible direction for future research is the development of more detailed mathematical formulations for protein dynamics. Another promising extension would be the inclusion of additional aspects of Alzheimer’s disease pathology, such as brain atrophy, tau protein misfolding, and impaired clearance pathways.

From a numerical perspective, an inherent drawback of the current model is its inability to automatically preserve the positivity of protein concentrations. The design of structure-preserving numerical schemes therefore represents a relevant avenue for future development. Moreover, a complete *a priori* analysis of the proposed numerical method would provide further theoretical insight into its stability and convergence properties. Finally, the introduction of local discontinuous Galerkin strategies could enhance the robustness of the numerical treatment, particularly in handling the nonlinear diffusion terms.

Acknowledgments

OASIS-3 provided the brain MRI images: Longitudinal Multimodal Neuroimaging: Principal Investigators: T. Beninger, D. Marcus, J. Morris; NIH P30 AG066444, P50 AG00561, P30 NS09857781, P01 AG026276, P01 AG003991, R01 AG043434, UL1 TR000448, R01 EB009352. AV-45 doses were provided by Avid Radiopharmaceuticals, a wholly-owned subsidiary of Eli Lilly.

Funding This work is partially funded by the European Union (ERC SyG, NEMESIS, project number 101115663). Views and opinions expressed are, however, those of the authors only and do not necessarily reflect those of the European Union or the European Research Council Executive Agency. Neither the European Union nor the granting authority can be held responsible for them. MC was funded in part by the Austrian Science Fund (FWF) project

10.55776/F65. PFA has been partially supported by ICSC—Centro Nazionale di Ricerca in High Performance Computing, Big Data, and Quantum Computing, funded by the European Union—NextGeneration EU. Further, this work was supported by the NSF CMMI Award 2320933 Automated Model Discovery for Soft Matter and by the ERC Advanced Grant 101141626 DISCOVER to EK. The present research is part of the activities of the Dipartimento di Eccellenza 2023–2027 grant, funded by MUR. The authors acknowledge the CINECA award under the ISCRA initiative, for the availability of high-performance computing resources and support under the project IsCc9_NeuroDG, PI M. Corti, 2025–2026. PFA and MC are members of INdAM-GNCS.

A Parameter values for test cases

Tables 1 and 2 below report the parameter values used in the simulations of Sections 4 and 5, respectively.

Parameter	Value	
$\mathbf{K}_A = k_A \mathbf{I}$	10^{-2}	$[\text{mm}^2 \cdot (\text{Pa} \cdot \text{s})^{-1}]$
$\mathbf{K}_V = k_V \mathbf{I}$	10^{-2}	$[\text{mm}^2 \cdot (\text{Pa} \cdot \text{s})^{-1}]$
k_C	5×10^{-3}	$[\text{mm}^2 \cdot (\text{Pa} \cdot \text{s})^{-1}]$
β_{AC}	5×10^{-7}	$[(\text{Pa} \cdot \text{s})^{-1}]$
β_{CV}	4×10^{-7}	$[(\text{Pa} \cdot \text{s})^{-1}]$
p_{Arteries}	70.00	[mmHg]
p_{Veins}	7.00	[mmHg]
k_C^{AB}	10^{-4}	$[\text{mm}^2 \cdot (\text{Pa} \cdot \text{s})^{-1}]$
α_{k_C}	2.00	[years]
β_{AC}^{AB}	4×10^{-7}	$[(\text{Pa} \cdot \text{s})^{-1}]$
$\alpha_{\beta_{AC}}$	2.00	[years]
β_{CV}^{AB}	3×10^{-7}	$[(\text{Pa} \cdot \text{s})^{-1}]$
$\alpha_{\beta_{CV}}$	2.00	[years]

(a) Physical parameters of perfusion equations

Parameter	Value	
d_{ext}	8.00	$[\text{mm}^2 \cdot \text{years}^{-1}]$
d_{axn}	0.00	$[\text{mm}^2 \cdot \text{years}^{-1}]$
k_1	1.00	$[\text{years}^{-1}]$
\tilde{k}_1	1.50	$[\text{years}^{-1}]$
k_0	1.00	$[\mu\text{g} \cdot \text{years}^{-1} \cdot \text{mm}^{-3}]$
k_{12}	1.00	$[\text{mm}^3 \cdot \mu\text{g}^{-1} \cdot \text{years}^{-2}]$
κ_1	1.25	$[\text{years}^{-1}]$
$\tilde{\kappa}_1$	3.75	$[\text{years}^{-1}]$
κ_0	1.25	$[\mu\text{g} \cdot \text{years}^{-1} \cdot \text{mm}^{-3}]$

(b) Physical parameters of heterodimer equations

Dimensionless Parameter	Healthy Value	Misfolded Value
$\sigma_A = \sigma_A (\bar{\mathbf{k}} \otimes \bar{\mathbf{k}})$	3.00×10^4	
$\sigma_V = \sigma_V (\bar{\mathbf{k}} \otimes \bar{\mathbf{k}})$	3.00×10^4	
B	0.75	
$\sigma_C = \sigma_C \mathbf{I}$	1.50×10^4	3.00×10^2
$\tilde{\gamma}_{CV}$	1.00	0.75
$\tilde{\gamma}_{AC}$	1.00	0.80

(c) Dimensionless parameters of perfusion equations

Dimensionless Parameter	Healthy Value	Misfolded Value
δ_{ext}		1.00
δ_{axn}		0.00
ϵ		1.50
R		0.66
λ_1^B	1.00	0.75
$\tilde{\lambda}_1^B$	1.00	0.50
μ_0^B	1.00	0.75

(d) Dimensionless parameters of heterodimer equations

Table 1: Test Cases of Section 4: Physical parameters appearing in Equation (14). The values are arbitrarily chosen for the simulation on the idealized geometry.

References

- [1] A. Ahern, T. B. Thompson, H. Oliveri, S. Lorthois, and A. Goriely. Modelling cerebrovascular pathology and the spread of amyloid beta in Alzheimer’s disease. *Proceedings of the Royal Society A: Mathematical, Physical and Engineering Sciences*, 481(2311):20240548, 2025.
- [2] E. C. Aifantis. Continuum basis for diffusion in regions with multiple diffusivity. *Journal of Applied Physics*, 50:1334, 1979.

Parameter	Value	
$\mathbf{K}_A = k_A (\bar{\mathbf{k}} \otimes \bar{\mathbf{k}})$	1.23×10^{-3}	$[\text{mm}^2 \cdot (\text{Pa} \cdot \text{s})^{-1}]$
$\mathbf{K}_V = k_V (\bar{\mathbf{k}} \otimes \bar{\mathbf{k}})$	1.23×10^{-3}	$[\text{mm}^2 \cdot (\text{Pa} \cdot \text{s})^{-1}]$
$\mathbf{K}_C = k_C \mathbf{I}$	4.28×10^{-7}	$[\text{mm}^2 \cdot (\text{Pa} \cdot \text{s})^{-1}]$
β_{AC}	1.00×10^{-6}	$[(\text{Pa} \cdot \text{s})^{-1}]$
β_{CV}	3.00×10^{-6}	$[(\text{Pa} \cdot \text{s})^{-1}]$
p_{Arteries}	70.00	[mmHg]
p_{Veins}	7.00	[mmHg]
k_C^{AB}	1.00×10^{-7}	$[\text{mm}^2 \cdot (\text{Pa} \cdot \text{s})^{-1}]$
α_{k_C}	2.50	[years]
β_{AC}^{AB}	8.00×10^{-7}	$[(\text{Pa} \cdot \text{s})^{-1}]$
$\alpha_{\beta_{AC}}$	2.50	[years]
β_{CV}^{AB}	2.40×10^{-6}	$[(\text{Pa} \cdot \text{s})^{-1}]$
$\alpha_{\beta_{CV}}$	2.50	[years]

(a) Physical parameters of perfusion equations.

Parameter	Value	
d_{ext}	8.00	$[\text{mm}^2 \cdot \text{years}^{-1}]$
d_{axn}	80.00	$[\text{mm}^2 \cdot \text{years}^{-1}]$
k_1	1.00	$[\text{years}^{-1}]$
\tilde{k}_1	1.50	$[\text{years}^{-1}]$
k_0	1.00	$[\mu\text{g} \cdot \text{years}^{-1} \cdot \text{mm}^{-3}]$
k_{12}	1.20	$[\text{mm}^3 \cdot \mu\text{g}^{-1} \cdot \text{years}^{-2}]$
κ_1	1.25	$[\text{years}^{-1}]$
$\tilde{\kappa}_1$	3.75	$[\text{years}^{-1}]$
κ_0	1.25	$[\mu\text{g} \cdot \text{years}^{-1} \cdot \text{mm}^{-3}]$

(b) Physical parameters of heterodimer equations.

Dimensionless Parameter	Healthy Value	Misfolded Value
$\sigma_A = \sigma_A (\bar{\mathbf{k}} \otimes \bar{\mathbf{k}})$	2.31×10^2	
$\sigma_V = \sigma_V (\bar{\mathbf{k}} \otimes \bar{\mathbf{k}})$	2.31×10^2	
B	3.00	
$\sigma_C = \sigma_C \mathbf{I}$	8.02×10^{-2}	1.87×10^{-2}
$\tilde{\gamma}_{CV}$	1.00	0.80
$\tilde{\gamma}_{AC}$	1.00	0.80

(c) Dimensionless parameters of perfusion equations.

Dimensionless Parameter	Healthy Value	Misfolded Value
δ_{ext}		1.00
δ_{axn}		10.00
ϵ		1.50
R		0.80
λ_1^B	1.00	0.75
$\tilde{\lambda}_1^B$	1.00	0.50
μ_0^B	1.00	0.75

(d) Dimensionless parameters of heterodimer equations.

Table 2: Test Cases of Section 5: Physical and dimensionless parameters of the model. The values of the parameters of the uncoupled problems of (a) from [31] and of (b) from [4].

- [3] C. G. Alexandersen, W. de Haan, C. Bick, and A. Goriely. A multi-scale model explains oscillatory slowing and neuronal hyperactivity in alzheimer's disease. *Journal of The Royal Society Interface*, 20(198):20220607, 2023.
- [4] P. F. Antonietti, F. Bonizzoni, M. Corti, and A. Dall'Olio. Discontinuous Galerkin approximations of the heterodimer model for protein-protein interaction. *Computer Methods in Applied Mechanics and Engineering*, 431:117282, 2024.
- [5] P. F. Antonietti, M. Corti, and G. Martinelli. Polytopal mesh agglomeration via geometrical deep learning for three-dimensional heterogeneous domains. *Mathematics and Computers in Simulation*, 241:335–353, 2026.
- [6] M. Bertsch, B. Franchi, N. Marcello, M. C. Tesi, and A. Tosin. Alzheimer's disease: a mathematical model for onset and progression. *Mathematical medicine and biology : a journal of the IMA*, 34(2):193–214, 2017.
- [7] G. S. Brennan, T. B. Thompson, H. Oliveri, M. E. Rognes, and A. Goriely. The role of clearance in neurodegenerative diseases. *SIAM Journal on Applied Mathematics*, 84(3):S172–S198, 2024.
- [8] M. Causemann, V. Vinje, and M. E. Rognes. Human intracranial pulsatility during the cardiac cycle: a computational modelling framework. *Fluids and Barriers of the CNS*, 19:84, 2022.
- [9] P. Chaggar, J. W. Vogel, A. P. Binette, T. B. Thompson, O. Strandberg, N. Mattsson-Carlgren, L. Karlsson, E. Stomrud, S. Jbabdi, S. Magon, et al. Personalised regional modelling predicts tau progression in the human brain. *PLoS Biology*, 23(7):e3003241, 2025.
- [10] M. Corti. Exploring tau protein and amyloid-beta propagation: a sensitivity analysis of mathematical models based on biological data. *Brain Multiphysics*, 7:100098, 2024.

[11] M. Corti, P. F. Antonietti, L. Dede', and A. M. Quarteroni. Numerical modeling of the brain poromechanics by high-order discontinuous Galerkin methods. *Mathematical Models and Methods in Applied Sciences*, 33(08):1577–1609, 2023.

[12] M. Corti, F. Bonizzoni, and P. F. Antonietti. Structure preserving polytopal discontinuous Galerkin methods for the numerical modeling of neurodegenerative diseases. *Journal of Scientific Computing*, 100(2):39, 2024.

[13] M. Corti, F. Bonizzoni, P. F. Antonietti, and A. M. Quarteroni. Uncertainty quantification for Fisher–Kolmogorov equation on graphs with application to patient-specific Alzheimer’s disease. *ESAIM: Mathematical Modelling and Numerical Analysis*, 58(6):2135–2154, 2024.

[14] M. Corti, F. Bonizzoni, L. Dede', A. M. Quarteroni, and P. F. Antonietti. Discontinuous Galerkin methods for Fisher–Kolmogorov equation with application to α -synuclein spreading in Parkinson’s disease. *Computer Methods in Applied Mechanics and Engineering*, 417:116450, 2023.

[15] J. C. Cruz Hernández, O. Bracko, C. J. Kersbergen, V. Muse, M. Haft-Javaherian, M. Berg, L. Park, L. K. Vinarcsik, I. Ivasyk, D. A. Rivera, Y. Kang, M. Cortes-Canteli, M. Peyrounette, V. Doyeux, A. Smith, J. Zhou, G. Otte, J. D. Beverly, E. Davenport, Y. Davit, C. P. Lin, S. Strickland, C. Iadecola, S. Lorthois, N. Nishimura, and C. B. Schaffer. Neutrophil adhesion in brain capillaries reduces cortical blood flow and impairs memory function in Alzheimer’s disease mouse models. *Nature Neuroscience*, 22(3):413–420, 2019.

[16] J. Eberling, W. Jagust, B. Reed, and M. Baker. Reduced temporal lobe blood flow in Alzheimer’s disease. *Neurobiology of Aging*, 13(4):483–491, 1992.

[17] S. Fantini, A. Sassaroli, K. Tgavalekos, and J. Kornbluth. Cerebral blood flow and autoregulation: current measurement techniques and prospects for noninvasive optical methods. *Neurophotonics*, 21(3):031411, 2016.

[18] B. Fischl. FreeSurfer. *NeuroImage*, 62(2):774–781, 2012.

[19] S. Fornari, A. Schäfer, E. Kuhl, and A. Goriely. Spatially-extended nucleation-aggregation-fragmentation models for the dynamics of prion-like neurodegenerative protein-spreading in the brain and its connectome. *Journal of Theoretical Biology*, 486:110102, 2020.

[20] S. Fornari, A. Schäfer, M. Jucker, A. Goriely, and E. Kuhl. Prion-like spreading of Alzheimer’s disease within the brain’s connectome. *Journal of The Royal Society Interface*, 16(159):20190356, 2019.

[21] B. Franchi and S. Lorenzani. From a microscopic to a macroscopic model for Alzheimer disease: two-scale homogenization of the Smoluchowski equation in perforated domains. *Journal of Nonlinear Science*, 24:717–753, 2016.

[22] M. Geodert. Alzheimer’s and Parkinson’s diseases: The prion concept in relation to assembled $A\beta$, tau, and α -synuclein. *Science*, 349:1255555, 2015.

[23] P. B. Gorelick, A. Scuteri, S. E. Black, C. Decarli, S. M. Greenberg, C. Iadecola, L. J. Launer, S. Laurent, O. L. Lopez, D. Nyenhuis, R. C. Petersen, J. A. Schneider, C. Tzourio, D. K. Arnett, D. A. Bennett, H. C. Chui, R. T. Higashida, R. Lindquist, P. M. Nilsson, G. C. Roman, F. W. Sellke, and S. Seshadri. Vascular contributions to cognitive impairment and dementia: A statement for healthcare professionals from the American Heart Association/American Stroke Association. *Stroke*, 42(9):2672–2713, 2011.

[24] A. Goriely, E. Kuhl, and C. Bick. Neuronal oscillations on evolving networks: dynamics, damage, degradation, decline, dementia, and death. *Physical Review Letters*, 125(12):128102, 2020.

[25] D. Heftner and A. Draguhn. APP as a protective factor in acute neuronal insults. *Frontiers in Molecular Neuroscience*, 10:22, 2017.

[26] C. Iadecola. Neurovascular regulation in the normal brain and in Alzheimer’s disease. *Nature Reviews Neuroscience*, 5(5):347–360, 2004.

[27] C. Iadecola. The pathobiology of vascular dementia. *Neuron*, 80(4):844–866, 2013.

[28] Y. Iturria-Medina, R. Sotero, P. Toussaint, J. Mateos-Pérez, A. Evans, and the Alzheimer’s Disease Neuroimaging Initiative. Early role of vascular dysregulation on late-onset Alzheimer’s disease based on multifactorial data-driven analysis. *Nature Communications*, 7:11934, 2016.

[29] T. Józsa, J. Petr, S. Payne, and H. Mutsaerts. MRI-based parameter inference for cerebral perfusion modelling in health and ischaemic stroke. *Computers in Biology and Medicine*, 166:107543, 2023.

[30] T. I. Józsa, R. M. Padmos, W. K. El-Bouri, A. G. Hoekstra, and S. J. Payne. On the sensitivity analysis of porous finite element models for cerebral perfusion estimation. *Annals of Biomedical Engineering*, 49(12):3647–3665, 2021.

[31] T. I. Józsa, R. M. Padmos, N. Samuels, W. K. El-Bouri, A. G. Hoekstra, and S. J. Payne. A porous circulation model of the human brain for in silico clinical trials in ischaemic stroke. *Interface Focus*, 11:20190127, 2021.

[32] R. N. Kalaria, R. Akinyemi, and M. Ihara. Does vascular pathology contribute to Alzheimer changes? *Journal of the Neurological Sciences*, 322(1-2):141—147, 2012.

[33] J. P. Keener. *Biology in time and space: a partial differential equation modeling approach*, volume 50. American Mathematical Soc., 2021.

[34] P. Kevrekidis, T. B. Thompson, and A. Goriely. Anisotropic diffusion and traveling waves of toxic proteins in neurodegenerative diseases. *Physics Letters A*, 384(36):126935, 2020.

[35] K. Kisler, A. Nelson, A. Montagne, and B. Zlokovic. Cerebral blood flow regulation and neurovascular dysfunction in Alzheimer disease. *Nature Reviews Neuroscience*, 18(7):419–434, 2017.

[36] N. Korte, R. Nortley, and D. Attwell. Cerebral blood flow decrease as an early pathological mechanism in Alzheimer’s disease. *Acta Neuropathologica*, 140(6):793–810, 2020.

[37] P. J. LaMontagne, T. L. Benzinger, J. C. Morris, S. Keefe, R. Hornbeck, C. Xiong, E. Grant, J. Hassenstab, K. Moulder, A. G. Vlassenko, M. E. Raichle, C. Cruchaga, and D. Marcus. OASIS-3: Longitudinal neuroimaging, clinical, and cognitive dataset for normal aging and Alzheimer disease, 2019.

[38] J. J. Lee, E. Piersanti, K.-A. Mardal, and M. E. Rognes. A mixed finite element method for nearly incompressible multiple-network poroelasticity. *SIAM Journal on Scientific Computing*, 41(2):A722–A747, 2019.

[39] C. L. Leimer Saglio, S. Pagani, and Antonietti. A p -adaptive polytopal discontinuous galerkin method for high-order approximation of brain electrophysiology. *Computer Methods in Applied Mechanics and Engineering*, 446:118249, 2025.

[40] Z. Li, D. Chen, Z. Li, H. Fan, L. Guo, B. Sui, and Y. Ventikos. A computational study of fluid transport characteristics in the brain parenchyma of dementia subtypes. *Journal of Biomechanics*, 159:111803, 2023.

[41] S. Love and J. S. Miners. Cerebrovascular disease in ageing and Alzheimer’s disease. *Acta Neuropathologica*, 131(5):645—658, 2016.

[42] K.-A. Mardal, M. E. Rognes, T. B. Thompson, and L. M. Valnes. *Mathematical Modeling of the Human Brain: From Magnetic Resonance Images to Finite Element Simulation*, volume 10. Springer International Publishing, 2022.

[43] S. Marks, S. Lockhart, S. Baker, and W. Jagust. Tau and β -Amyloid are associated with medial temporal lobe structure, function, and memory encoding in normal aging. *The Journal of Neuroscience*, 37(12):3192–3201, 2017.

[44] F. Matthäus. Diffusion versus network models as descriptions for the spread of prion diseases in the brain. *Journal of Theoretical Biology*, 240(1):104–113, 2006.

[45] K. Niwa, V. A. Porter, K. E. Kazama, D. Cornfield, G. A. Carlson, and C. Iadecola. $\text{A}\beta$ -peptides enhance vasoconstriction in cerebral circulation. *American Journal of Physiology - Heart and Circulatory Physiology*, 281(6):2417–2424, 2001.

[46] R. Nortley, N. Korte, P. Izquierdo, C. Hirunpattarasilp, A. Mishra, Z. Jaumuktane, V. Kyrgargyri, T. Pfeiffer, L. Khennouf, C. Madry, H. Gong, A. Richard-Loendt, W. Huang, T. Saito, T. C. Saido, S. Brandner, H. Sethi, and D. Attwell. Amyloid β oligomers constrict human capillaries in Alzheimer’s disease via signaling to pericytes. *Science*, 365(6450):eaav9518, 2019.

[47] V. Pederzoli, M. Corti, D. Riccobelli, and P. F. Antonietti. A coupled mathematical and numerical model for protein spreading and tissue atrophy applied to Alzheimer's disease. *Computer Methods in Applied Mechanics and Engineering*, 444:118118, 2025.

[48] M. Peyrounette, Y. Davit, M. Quintard, and S. Lorthois. Multiscale modelling of blood flow in cerebral microcirculation: Details at capillary scale control accuracy at the level of the cortex. *Plos One*, 13(1):e0189474, 2018.

[49] E. Piersanti, J. Lee, T. Thompson, K.-A. Mardal, and M. Rognes. Parameter robust preconditioning by congruence for multiple-network poroelasticity. *SIAM Journal on Scientific Computing*, 43:B984–B1007, 2021.

[50] S. B. Prusiner. Molecular biology of prion diseases. *Science*, 252(5012):1515–1522, 1991.

[51] A. M. Quarteroni. *Numerical Models for Differential Problems*, volume 8. Springer International Publishing, 2013.

[52] A. E. Roher, C. Esh, A. Rahman, T. A. Kokjohn, and T. G. Beach. Atherosclerosis of cerebral arteries in Alzheimer disease. *Stroke*, 35(11 suppl. 1):2623—2627, 2004.

[53] A. P. Sagare, R. D. Bell, and B. V. Zlokovic. Neurovascular dysfunction and faulty amyloid β -peptide clearance in Alzheimer disease. *Cold Spring Harbor Perspectives in Medicine*, 2(10):1–18, 2012.

[54] P. Scheltens, B. De Strooper, M. Kivipelto, H. Holstege, G. Chételat, C. E. Teunissen, J. Cummings, and W. M. van der Flier. Alzheimer's disease. *The Lancet*, 397:1577–1590, 2021.

[55] F. Schmid, P. S. Tsai, D. Kleinfeld, P. Jenny, and B. Weber. Depth-dependent flow and pressure characteristics in cortical microvascular networks. *PLOS Computational Biology*, 13(2):e1005392, 2017.

[56] A. Schäfer, J. Weickenmeier, and E. Kuhl. The interplay of biochemical and biomechanical degeneration in Alzheimer's disease. *Computer Methods in Applied Mechanics and Engineering*, 352:369–388, 2019.

[57] J. Shi, K. S. Panickar, S.-H. Yang, O. Rabbani, A. L. Day, and J. W. Simpkins. Estrogen attenuates overexpression of β -amyloid precursor protein messenger RNA in an animal model of focal ischemia. *Brain research*, 810(1-2):87—92, 1998.

[58] J. Shi, S. H. Yang, L. Stuble, A. L. Day, and J. W. Simpkins. Hypoperfusion induces overexpression of β -amyloid precursor protein mRNA in a focal ischemic rodent model. *Brain Research*, 853(1):1–4, 2000.

[59] H. M. Snyder, R. A. Corriveau, S. Craft, J. E. Faber, S. M. Greenberg, D. Knopman, B. T. Lamb, T. J. Montine, M. Nedergaard, C. B. Schaffer, J. A. Schneider, C. Wellington, D. M. Wilcock, G. J. Zipfel, B. Zlokovic, L. J. Bain, F. Bosetti, Z. S. Galis, W. Koroshetz, and M. C. Carrillo. Vascular contributions to cognitive impairment and dementia including Alzheimer's disease. *Alzheimer's and Dementia*, 11(6):710–717, 2015.

[60] X. Sun, G. He, H. Qing, W. Zhou, F. Dobie, F. Cai, M. Staufenbiel, L. E. Huang, and W. Song. Hypoxia facilitates Alzheimer's disease pathogenesis by up-regulating BACE1 gene expression. *Proceedings of the National Academy of Sciences*, 103(49):18727–18732, 2006.

[61] D. Thal, U. Rub, M. Orantes, and H. Braak. Phases of a beta-deposition in the human brain and its relevance for the development of AD. *Neurology*, 58(12):1791–1800, 2002.

[62] T. Thomas, G. Thomas, C. McLendon, T. Sutton, and M. Mullan. β -amyloid-mediated vasoactivity and vascular endothelial damage. *Nature*, 380(6570):168–171, 1996.

[63] T. B. Thompson, P. Chaggar, E. Kuhl, A. Goriely, and ADNI. Protein-protein interactions in neurodegenerative diseases: A conspiracy theory. *PLOS Computational Biology*, 16(10):e1008267, 2020.

[64] B. J. Tully and Y. Ventikos. Cerebral water transport using multiple-network poroelastic theory: application to normal pressure hydrocephalus. *Journal of Fluid Mechanics*, 667:188–215, 2011.

[65] J. C. Vardakas, D. Chou, L. Guo, and Y. Ventikos. Exploring neurodegenerative disorders using a novel integrated model of cerebral transport: Initial results. *Proceedings of the Institution of Mechanical Engineers, Part H: Journal of Engineering in Medicine*, 234(11):1223–1234, 2020.

- [66] J. Weickenmeier, M. Jucker, A. Goriely, and E. Kuhl. A physics-based model explains the prion-like features of neurodegeneration in Alzheimer's disease, Parkinson's disease, and amyotrophic lateral sclerosis. *Journal of the Mechanics and Physics of Solids*, 124:264–281, 2019.
- [67] J. Weickenmeier, E. Kuhl, and A. Goriely. Multiphysics of prionlike diseases: Progression and atrophy. *Physical Review Letters*, 121(15):158101, 2018.
- [68] X. Zhang, K. Zhou, R. Wang, J. Cui, S. A. Lipton, F.-F. Liao, H. Xu, and Y.-w. Zhang. Hypoxia-inducible factor 1 α (HIF-1 α)-mediated hypoxia increases BACE1 expression and β -amyloid generation. *Journal of Biological Chemistry*, 282(15):10873–10880, 2007.
- [69] B. V. Zlokovic. Neurovascular pathways to neurodegeneration in Alzheimer's disease and other disorders. *Nature Reviews Neuroscience*, 12(12):723—738, 2011.